*Supplementary Information of*

# Global Nitrous Oxide Budget 1980-2020

**Hanqin Tian et al.**

*Correspondence to:* Hanqin Tian (hanqin.tian@bc.edu)

# Extended methodology

**SI-1 NMIP-2**: global **N**itrogen/$N_2O$ **M**odel **I**nter-comparison **P**roject phase **2**

The NMIP2 is a follow-up model intercomparison project of NMIP (*Tian et al.*, 2018), which provides estimates of $N_2O$ emissions from natural and agricultural soils and covers the time period 1850-2020. Eight process-based Terrestrial Biosphere Models (TBMs) participate in NMIP-2. In general, $N_2O$ emissions from soil are regulated at two levels, which are the rates of nitrification and denitrification in the soil and soil physical factors regulating the ratio of $N_2O$ to other nitrous gases (*Davidson et al.*, 2000). For N input to land ecosystems, all eight models considered N fertilizer use, atmospheric N deposition and biological fixation, but six models considered manure as N input. For vegetation processes, all models included dynamic algorithms in simulating N allocation to different living tissues and vegetation N turnover, and simulated plant N uptake using the "Demand and Supply-driven" approach. For soil N processes, all eight models simulated N leaching according to water runoff rate; however, models are different in representing nitrification and denitrification processes and the impacts of soil chemical and physical factors. The differences in simulating nitrification and denitrification processes are one of the major uncertainties in estimating $N_2O$ emissions. Model characteristics in simulating major N cycling processes associated with $N_2O$ emissions in each participating model are briefly described in Table SI-1.

**Table SI-1. Model characteristics in simulating major N cycling processes**

| | CLASSIC | DLEM | ELM | ISAM | LPX-Bern | O-CN | ORCHIDEE | VISIT |
|---|---|---|---|---|---|---|---|---|
| Open C cycle [a] | Yes | Yes | Yes | Yes | Yes | Yes | Yes | Yes |
| C-N coupling | Yes | Yes | Yes | Yes | Yes | Yes | Yes | Yes |
| N pools [b] | (3, 1, 3) | (6,6,8) | (6,4,5) | (6,4,4) | (4,3,8) | (9,6,9) | (9,6,9) | (4,1,4) |
| Demand and supply–driven plant N uptake | Yes | Yes | Yes | Yes | Yes | Yes | Yes | Yes |
| N allocation [c] | Dynamic | Dynamic | Dynamic | Dynamic | Dynamic | Dynamic | Dynamic | Dynamic |
| Nitrification | *f(T, SWC, $C_{NH4}$)* | *f(T, SWC, $C_{NH4}$)* | *f(T, SWC, pH, rh, $C_{NH4}$)* | *f(T, SWC, $C_{NH4}$)* | *f(T, SWC, $C_{NH4}$)* | *f(T, SWC, pH, $C_{NH4}$)* | *f(T, SWC, pH, $C_{NH4}$)* | *f(T, SWC, pH, $C_{NH4}$)* |
| Denitrification | *f(T, SWC, $C_{NO3}$)* | *f(T, SWC, clay, rh, $C_{NO3}$)* | *f(T, SWC, pH, rh, $C_{NO3}$)* | *f(T, SWC, $C_{NO3}$)* | *f(T, SWC, $R_{mb}$, $C_{NO3}$)* | *f(T, SWC, pH, $R_{mb}$, $C_{NO3}$)* | *f(T, SWC, pH, denitrifier, $C_{NO3}$)* | *f(SWC, rh, $C_{NO3}$)* |
| Mineralization, immobilization | *f(C:N)* | *f(C:N)* | *f(C:N)* | *f(C:N)* | *f(C:N)* | *f(C:N)* | *f(C:N)* | *f(C:N)* |
| N leaching | *f(runoff, $C_{NO3}$, $C_{NH4}$)* | *f(runoff, $C_{NO3}$, $C_{NH4}$)* | *f(runoff, $C_{NO3}$)* | *f(runoff, $C_{NO3}$, $C_{NH4}$)* | *f(runoff, $C_{NO3}$)* | *f(runoff, $C_{NO3}$, $C_{NH4}$)* | *f(runoff, $C_{NO3}$, $C_{NH4}$)* | *f(runoff, $C_{NO3}$)* |
| $NH_3$ volatilization | *f($C_{NH3}$)* | *f(T, SWC, pH, $C_{NH4}$)* | No | *f($C_{NH3}$)* | *f(T, SWC, pH, $C_{NH4}$)* | *f($C_{NH3}$)* | *f(SWC, pH, $C_{NH4}$)* | *f(T, SWC, pH, $C_{NH4}$)* |
| Plant N turnover [d] | Dynamic | Dynamic | Dynamic | Dynamic | Dynamic | Dynamic | Dynamic | Dynamic |
| N resorption | Fixed | *f(C:N)* | Fixed | *f(C:N)* | Fixed | Fixed | Fixed | Fixed |
| N fixation | *f($N_{limit}$)* | *f(T, SWC, $C_{NH4}$, $C_{NO3}$)* | *f(T, C:N)* | *f(ET)* | Implied by mass balance | *f($N_{limit}$)* | Fixed | *f(ET)* |
| N fertilizer use | Yes | Yes | Yes | Yes | Yes | Yes | Yes | Yes |
| Manure N use | No | Yes | No | Yes | No | Yes | Yes | Yes |
| N deposition | Yes | Yes | Yes | Yes | Yes | Yes | Yes | Yes |

[a] *"Open" denotes that excess N can be leached from the system.*
[b] *Numbers of N pools (vegetation pools, litter pools, soil pools).*
[c] *Dynamic denotes time-varied N allocation ratio to different N pools.*

*T: soil temperature, SWC: soil water content, clay: soil clay fraction, ET: evapotranspiration, denitrifier: soil denitrifier biomass, rh: soil heterogeneous respiration, Nlimit: N limitation of vegetation growth,* $C_{NO3}$*: soil* $NO_3^-$ *content,* $C_{NH4}$*: soil* $NH_4^+$ *content.*

All NMIP2 models are driven by consistent input datasets (i.e., climate, atmospheric $CO_2$ concentration, land cover change, irrigation, atmospheric N deposition, mineral N fertilization, and manure N application and deposition) and implemented consistent simulation experiments (SH0 – SH12; Table A4). Nitrogen inputs data used in NMIP2 simulations are from History of anthropogenic Nitrogen inputs (HaNi) dataset (*Tian et al.*, 2022), which takes advantage of different data sources in a spatiotemporally consistent way to generate a set of high-resolution (5 arcminutes) gridded N input products from 1850 to 2020. HaNi data set shows that the total anthropogenic N inputs to global terrestrial ecosystems increased from 29.05 Tg N $yr^{-1}$ in the 1860s to 267.23 Tg N $yr^{-1}$ in the 2010s, with the dominant N source changing from atmospheric N deposition (before the 1900s) to manure N (the 1910s-2000s), and to synthetic fertilizer in the 2010s (Fig. B3). The climate data used to run historical simulations is the half degree CRU-JRA2.2 6-hourly forcing over 1901- 2020 (https://catalogue.ceda.ac.uk/uuid/4bdf41fc10af4caaa489b14745c665a6). Annual $CO_2$ concentration during 1850-2020 were derived from ice core $CO_2$ data and NOAA annual observations(https://www.esrl.noaa.gov). Historical distribution of cropland, pasture, rangeland and irrigation during 1850-2020 were from Land-Use Harmonization 2 (LUH2) dataset (*Hurtt et al.*, 2020). The original dataset of LUH2 is at a resolution of 0.25° x 0.25° longitude/latitude. We aggregated all geo-referenced input data into a consistent spatial resolution of 0.5° x 0.5° longitude/latitude to run NMIP2 models.

NMIP2 models perform a subset of 13 simulations (SH0-SH12) to quantify $N_2O$ emissions from both agricultural and natural soils during the study period, and to disentangle the effects of multiple environmental factors on soil $N_2O$ emissions. The SH1 results were taken as the "best estimates" of soil $N_2O$ emissions because they include the effects of all driving factors that models can take into account. In the SH0 simulation, driving forces were kept constant at the level in 1850 over the entire simulation period (1850-2020). According to previous $N_2O$ budget studies, atmospheric $N_2O$ growth rate and Monte-Carlo method, we suggest the following criteria for the $N_2O$ budget inclusion (Table A6), and the criteria for carbon components are consistent with TRENDY. By comparing results from factorial simulation experiments (SH0 - SH12), we attribute changes in soil $N_2O$ emissions to seven natural and anthropogenic factors, namely, climate (CLIM, including precipitation, humidity, temperature and photosynthetic active radiation changes), atmospheric $CO_2$ concentration ($CO_2$), land cover change (LCC), irrigation (IRRI), atmospheric N deposition (NDEP), mineral N fertilizer use (NFER), and manure N use in cropland (MANN). In order to understand soil $N_2O$ emissions dynamics caused by crop cultivation, we further separate the global and regional $N_2O$ emissions into those derived from cropland soils and those from soils of other land ecosystems. In this study, we attribute the impact of a single factor on cropland $N_2O$ emissions. Five models (DLEM, ISAM, O-CN, ORCHIDEE, and VISIT) considered the effects of manure N application in cropland, therefore, we use these five models' results to calculate the manure N effect (SH1-SH2). Meanwhile, we used results from all the eight models (i.e., CLASSIC, DLEM, ELM, ISAM, LPX-Bern, O-CN, ORCHIDEE, and VISIT) to calculate the effects of synthetic N fertilizer use (SH1-SH3) and atmospheric N deposition (SH1-SH4). The effect of N deposition in natural ecosystems (SH1-SH4) and the effects of $CO_2$ (SH1-SH7) and climate (SH1-SH8) on global terrestrial ecosystems are calculated from the eight NMIP2 models mentioned above.

**Table SI-2. Criteria for the $N_2O$ budget inclusion**

| Carbon criteria | $N_2O$ criteria |
| --- | --- |
| (1) Steady state after spin-up, diagnosed from SH0 run: steady-state defined as an offset < 0.10 PgC $yr^{-1}$, drift < 0.05 PgC $yr^{-1}$ per century (i.e. first is the average over 1850-2020, second is the slope x 100). | (1) Steady state after spin-up, diagnosed from SH0 run: drift < 0.2 Tg $N_2O$-N $yr^{-1}$ per century (i.e. the slope x 100). |
| (2) Net annual land flux is a carbon sink over the 1990s and 2000s as constrained by global atmospheric and oceanic observations (Keeling & Manning, 2014), diagnosed from SH3 run. | (2) Inside the present-day (2007-2016) land emission range: 7-13 Tg $N_2O$-N $yr^{-1}$, diagnosed from SH1 run. The upper limit was calculated using the maximum total $N_2O$ emissions minus the minimum estimates of other sources, and the lower limit was calculated using the minimum total $N_2O$ emissions minus the maximum estimates of other sources. The range of total emissions was estimated by a one-box model using atmospheric $N_2O$ growth rate, and the range of the sum of other sources was calculated by a Monte-Carlo method using estimates from Tian et al. (2020). |
| | (3) Inside the pre-industrial land emission range: 3 to 9 Tg $N_2O$-N $yr^{-1}$, diagnosed from SH1 run. This range is derived from the pre-industrial atmospheric burden/$N_2O$ lifetime minus ocean and river/ coastal/estuary emissions (Michael J. Prather et al., 2015). |

**Brief description of algorithms associated with $N_2O$ flux in each NMIP2 model:**

**1: CLASSIC**

The representation of nitrogen cycling in CLASSIC is described in *Asaadi and Arora* (2021) and *Kou Giesbrecht and Arora* (2022). $N_2O$ production due to both nitrification and denitrification are represented. $N_2O$ loss during nitrification (; g N $m^{-2}$ $d^{-1}$) is represented with the following equation:

is a coefficient ($d^{-1}$), is a dimensionless scalar that depends on soil temperature averaged over the top 0.5m soil depth, is a dimensionless scalar that depends on soil matric potential, and is the soil ammonium pool (g N $m^{-2}$).

$N_2O$ loss during denitrification (; g N $m^{-2}$ $d^{-1}$) is represented with the following equation:

is a coefficient ($d^{-1}$), is a dimensionless scalar that depends on soil temperature averaged over the top 0.5m soil depth, is a dimensionless scalar that depends on soil moisture (), and is the soil nitrate pool (g N $m^{-2}$).

**2: DLEM**

The nitrogen cycle scheme in DLEM2.0 (*Xu et al.*, 2017; *Yang et al.*, 2015) are similar as DLEM1.0 (*Lu and Tian*, 2013; *Tian et al.*, 2012b; *Tian et al.*, 2010; *Tian et al.*, 2011; *Xu et al.*, 2011), However, the $N_2O$ emission schemes in DLEM2.0 (*Xu et al.*, 2017) have been modified based on *Chatskikh et al.* (2005) and *Heinen* (2006).

$$R_{nit} = k_{nit\_max} f(T1) f(WFPS) C_{NH4} \quad (1)$$

$$R_{den} = k_{den\_max} f(T2) f(WFPS) C_{NO3} \quad (2)$$

where $R_{nit}$ is the daily nitrification rate (g N/$m^2$/d); $R_{den}$ is the daily denitrification rate (g N/$m^2$/d); $f(T1)$ and $f(T2)$ are the impact function of daily soil temperature on nitrification and denitrification, respectively; $f(WFPS)$ is the impact function of water-filled pore space (WFPS) on nitrification, denitrification and $N_2O$ diffusion; $k_{nit\_max}$ is the maximum fraction of $NH_4^+$-N that is converted to $NO_3^-$-N or gases (0-1); $k_{den\_max}$ is the maximum fraction of $NO_3^-$-N that is converted to gases (0-1); $C_{NH4}$ and $C_{NO3}$ are the soil $NH_4^+$-N and $NO_3^-$-N content (g N/$m^2$). $N_2O$ from denitrification and nitrification processes are calculated as,

$$R_{N2O} = (R_{nit} + R_{den}) f(T3)(1 - f(WFPS)) \quad (3)$$

where $R_{N2O}$ is the daily $N_2O$ emission rate (g N/$m^2$/d); $f(T3)$ is the impact function of daily soil temperature on $N_2O$ diffusion rate from soil pores. The calculation methods for these functions and parameters were described in detail in *Xu et al.* (2017) and *Yang et al.* (2015).

**3: ELM**

The nitrogen dynamics in ELM is simulated based on the theory of equilibrium chemistry approximation (*Zhu et al.*, 2016). Plants, soil microbes, and abiotic factors such as mineral surfaces coexist in the same soil environment and vie for a diverse array of nutrients, including NH4+, NO3-. Due to the limited availability of these nutrients, intense competitive interactions are expected. When the potential nutrient demands (from all nutrient consumers) exceed the supply at a given time step, the allocation of limited nutrients among the consumers affects their performance (e.g., plant growth, soil organic matter accumulation, nitrification, denitrification rates). ELM adopts a multiple-consumer-multiple-substrate competition network (Zhu et al., 2015; Zhu et al., 2019) to simulate (1) nitrogen uptake facilitated by nitrogen carrier enzymes, (2) binding of a nutrient substrate to a particular enzyme precludes it from attaching to other enzymes, and (3) rates and affinities of consumers for different substrates. After the nutrient competition has been resolved, scaling terms ($f(ECA_{nit})$ and $f(ECA_{den})$) will be applied to the potential nitrification and denitrification processes:

$$R_{nit} = k_{nit\_max} f(\theta) f(T)(1 - f(O)) f(ECA_{nit}) C_{NH4} \quad (4)$$

$$R_{den} = min\ (f(deomp), f(C_{NO3}))f(ECA_{den}) \quad (5)$$

where $k_{nit\_max}$ is the maximum nitrification rate, $f(\theta)$, $f(T)$, $f(O)$ are soil moisture, temperature, and oxygen scalars, respectively. $f(deomp)$ and $f(C_{NO3})$ are carbon limited and NO3- limited denitrification rates (*Del Grosso et al.*, 2000).

## 4: ISAM

ISAM model contains detailed calculations of the terrestrial ecosystem's organic and mineral N cycle (*Yang et al.*, 2009). The major N processes in ISAM include biological fixation, leaching, mineralization and immobilization, plant uptake, nitrification, and denitrification. The soil biogeochemistry module of ISAM shares the same ten soil layers (to 3.5 m depth) as the soil biogeophysics and calculates the vertical transport of SOC and N (*Shu et al.*, 2020; *Yang et al.*, 2009). $N_2O$ emission in ISAM $N_2O$ is produced as a byproduct of nitrification and denitrification (*Xu et al.*, 2021). $N_2O$ module explicitly accounts for the vertical transport of C, N, and $O_2$ within every soil layer for both saturated and unsaturated soil conditions by accounting for the process of oxygen diffusing into the soil from the atmosphere and the soil oxygen supply. The model also explicitly accounts for the effects of anoxic and oxic environments on nitrification ($N_{ni}$, Eq. 6) and denitrification ($N_{de}$, Eq. 7). Both environments are calculated based on the fraction of anoxic soil depending on soil $O_2$ concentration, which is non-linearly correlated with the chemical pathways forming $N_2O$.

$$N_{ni} = NH_4^+ \times (1 - e^{-F_{te\_m} \times F_{sm\_m} \times r_{ni}}) \times F_{pH\_m\_ni} \times\ R_d \quad (6)$$

$$N_{de} = NO_3^-\ \times r_{de} \times Rh \times F_{pH\_m\_de} \times R_d \quad (7)$$

where $NH_4^+$ and $NO_3^-$ are ammonium and nitrate pool sizes; $F_{te\_m}$ is temperature modifier; $F_{sm\_m}$ is soil moisture modifier; $r_{ni}$ and $r_{de}$ are base nitrification and denitrification rates; $F_{pH\_m\_ni}$ and $F_{pH\_m\_de}$ are pH modifiers for nitrification and denitrification; $R_d$ is relative soil anoxic fraction; *Rh* (= 1-$R_d$)is heterotrophic respiration.

Under anoxic soil conditions, $N_2O$ is produced through denitrification, while under oxic soil conditions, more $N_2O$ is produced from nitrification. The model accounts for soil $NH_4^+$ volatilization at the soil surface when $NH_4^+$ in $NH_4^+$-containing fertilizers (e.g., urea) is converted to ammonia gas, depending upon pH (*Huang and Gerber*, 2015). The soil $NH_4^+$ volatilization in the model is also affected by the anoxic condition, which increases under a higher temperature and relatively lesser soil anoxic condition. The model accounts for the impacts of pH on nitrification, denitrification, and volatilization rates (*Li et al.*, 2000; *Xu-Ri and Prentice*, 2008). We prescribe the soil pH from the Global Soil Dataset for Earth System Modeling dataset (GSDE) (*Shangguan et al.*, 2014).

## 5: LPX-Bern

The implementation of nitrogen dynamics in LPX-Bern is based on the work of *Xu-Ri and Prentice* (2008). Nitrogen uptake by plants is governed by their demand and the availability of nitrogen in two soil pools representing ammonium and nitrate. Nitrogen from deposition and fertilization are added to these inorganic soil pools. Losses include ammonium volatilization, nitrate leaching as well as $N_2O$ and NO production during nitrification and $N_2O$, NO and $N_2$ production during denitrification. Aerobic nitrification of ammonium is dependent on soil temperature ($T_{soil}$) and indirectly on soil water content due to the partitioning of wet and dry soil:

$$R_{nit} = max_{nit} f_1(T_{soil}) C_{NH4,dry} \quad (8)$$

where $max_{nit} = 0.92\ day^{-1}$ is the daily maximum nitrification rate at 20°C. Anaerobic denitrification of nitrate in wet soil depends on labile carbon availability and soil temperature:

$$R_{den} = R_{mb}/(R_{mb} + K_{mb}) f_2(T_{soil}) C_{NO3,wet}/(C_{NO3,wet} + K_n) \quad (9)$$

The parameters $K_{mb}$ and $K_n$ are taken from *Xu-Ri and Prentice* (2008) and $R_{mb}$ is the microbiotical soil respiration. The amount of nitrogen lost as $N_2O$ due to nitrification and denitrification is modelled as a function of soil temperature, water content and the respective process rate.

**6: O-CN**

The treatment of inorganic soil nitrogen dynamics in O-CN follows largely *Xu-Ri and Prentice* (2008). O-CN (*Zaehle and Friend*, 2010) considers N losses to $NH_3$ volatilisation, NOx, $N_2O$ and $N_2$ production and emission, as well as $NH_4$ and $NO_3$ leaching. Inorganic nitrogen dynamics in the soil are tightly coupled to plant uptake and net mineralization. The anaerobic volume fraction of the soil is estimated by an empirical function of the fractional soil moisture content (*Zaehle et al.*, 2011). The fraction of ammonium in the aerobic part of the soil is subject to nitrification, according to:

$$R_{nit} = vmax_{nit} f(T1) f(pH1) C_{NH4} \quad (10)$$

where *f(pH1)* is the soil pH response functions for nitrification (*Li et al.*, 1992; *Xu-Ri and Prentice*, 2008), and $vmax_{nit}$ is the maximum daily nitrification rate under 20°C and favourable pH conditions (*Xu-Ri and Prentice*, 2008).

Gross denitrification of the fraction of nitrate under anoxic conditions is modelled as:

$$R_{den} = R_{mb}/(R_{mb} + K_{mb}) f(T2) f(pH2) C_{NO3}/(C_{NO3} + K_n) \quad (11)$$

where *f(pH2)* is the soil pH response functions for denitrification (*Li et al.*, 1992; *Xu-Ri and Prentice*, 2008), $R_{mb}$ is the soil microbial respiration rate, and $K_{mb}$ and $K_n$ parameters taken from *Li et al.* (1992).

The $N_2O$ production from nitrification and denitrification is then calculated as:

$$R_{N2O} = a_{nit} f(T1) R_{nit} + b_{den} f(T2) f(pH3) R_{den} \quad (12)$$

where $a_{nit}$ and $b_{denit}$ are fraction loss constants, *f(pH3)* is a pH-modifier changing the degree of denitrification producing $N_2O$ versus $NO_x$ or $N_2$ (*Zaehle et al.*, 2011). Emissions of volatile compounds are simulated using the empirical emission of *Xu-Ri and Prentice* (2008).

**7: ORCHIDEE**

Modeling of the mineral N dynamics by the ORCHIDEE model originates from the formulations used in the O-CN (*Zaehle and Friend*, 2010). It is composed of five pools for ammonium/ammoniac, nitrate, NOx, nitrous oxide, and di-nitrogen forms. $N_2O$ production in both nitrification and denitrification processes are represented.

The potential daily rate of nitrification, $R_{nit}$, occurs only on the aerobic fraction of the soil and is a function of temperature, pH, and ammonium concentration ($C_{NH4}$):

$$R_{nit} = (1 - f(WFPS))f(T1)f(pH1)k_{nit}C_{NH4} \tag{13}$$

where $k_{\mathrm{nit}}$ is the reference potential $NO3^-$ production per mass unit of ammonium.

**8: VISIT**

The nitrogen cycle scheme of VISIT is composed of three organic soil nitrogen pools (microbe, litter, and humus), two inorganic soil nitrogen pools (ammonium and nitrate), and vegetation pools. Fertilizer is considered as an input to the ammonium and nitrate pools at a fixed ratio, and manure as an input into the litter organic nitrogen pool. $N_2O$ emissions through nitrification and denitrification are estimated using the scheme developed by *Parton et al.* (1996). Nitrification-associated $N_2O$ emission ($R_{nit,N2O}$) is evaluated as follows,

$$R_{nit,N2O} = f(WFPS)f(pH1)f(T1)(K_{max} + F_{max}f(NH4)) \tag{14}$$

where $K_{max}$ is the soil-specific turnover coefficient; $F_{max}$ is the parameter of maximum nitrification gas flux; and $f(NH_4)$ is the effect of soil ammonium on nitrification. Denitrification-associated $N_2O$ emission ($R_{den,N2O}$) is evaluated by the following equation:

$$R_{den,N2O} = R_{den}(1 + R_{N2/N2O}) \tag{15}$$

$$R_{den} = min\ (f(NO_3), f(CO_2)) \times f(WFPS) \tag{16}$$

where $R_{N2/N2O}$ is the fractionation coefficient, which is also a function of WFPS, soil nitrate, and heterotrophic respiration, $f(NO_3)$ is the maximum denitrification rate in high soil respiration rate condition, $f(CO_2)$ is the maximum denitrification rate in high $NO_3^-$ levels, and $f(WFPS)$ is the effect of WFPS on denitrification rate.

$N_2O$ production by nitrification ($R_{N2O,nit}$, g $N\text{-}N_2O/m^2/d$) is expressed as a function of the potential daily rate of nitrification ($R_{nit}$, g $N\text{-}NO_3^-/m^2/d$), temperature and the water content as shown in *Zhang et al.* (2002).

$$R_{N2O,nit} = f(WFPS)f(T1)R_{nit}p_{N2O,nit} \tag{17}$$

where $p_{N2O,nit}$ (g N-$N_2O$ (g N-$NO_3^-$)$^{-1}$) is the reference $N_2O$ production per mass unit of $NO_3^-$ produced by nitrification. The denitrification occurs on the anaerobic fraction of the soil which is computed as a function of the water-filled porosity (*f*(*WFPS*)) and is controlled by temperature, pH, soil NO concentration and denitrifier microbial activity ($a_{microb}$, g $m^{-2}$) (*Li et al.*, 2000).

$$R_{N2O,den} = f(WFPS)f(T2)f(pH)f(NO)p_{N2O,den}a_{microb} \quad (18)$$

where *f(NO)* is a Michaelis-Menten shape function and $p_{N2O,den}$ is the reference $N_2O$ production per mass unit of denitrifier microbes.

## SI-2 The FAOSTAT inventory

The FAOSTAT emissions data (*FAO*, 2022) are computed at Tier 1 following *IPCC* (2006), Vol.

4. The overall equation is as follows:
Direct emissions are estimated at the country level, using the formula:

$$Emission = A * EF \quad (19)$$

where emission represents kg N $yr^{-1}$; *A* represents the amount of N in the following items (annual synthetic N applications/manure applied to soils/manure left on pasture/manure treated in manure management systems/crop residue/biomass burned amount) in kg N $yr^{-1}$; *EF* = Tier 1, default IPCC emission factors, expressed in kg N/kg N.

Indirect emissions are estimated at the country level, using the formula:

$$Emission = A_{v\&l} * EF \quad (20)$$

where emission represents kg N $yr^{-1}$; $A_{v\&l}$ represents the fraction of manure/synthetic N fertilizers that volatize as $NH_3$ and $NO_x$ and are lost through runoff and leaching in kg N $yr^{-1}$; *EF* = Tier 1, default IPCC emission factors, expressed in kg N/kg N.

Synthetic N fertilizers: $N_2O$ from synthetic fertilizers is produced by microbial processes of nitrification and denitrification taking place on the addition site (direct emissions), and after volatilization/redeposition and leaching processes (indirect emissions).

Manure management: The term manure includes both urine and dung (i.e., both liquid and solid material) produced by livestock. $N_2O$ is produced directly by nitrification and denitrification processes in the manure, and indirectly by nitrogen (N) volatilization and redeposition processes.
Manure applied to soils: $N_2O$ is produced by microbial processes of nitrification and denitrification taking place on the application site (direct emissions), and after volatilization/redeposition and leaching processes (indirect emissions).

Manure left on pastures: $N_2O$ is produced by microbial processes of nitrification and denitrification taking place on the deposition site (direct emissions), and after volatilization/redeposition and leaching processes (indirect emissions).

Crop Residue: $N_2O$ emissions from crop residues consist of direct and indirect emissions from nitrogen (N) in crop residues left on agricultural fields by farmers and from forages during pasture renewal (following the definitions in the IPCC guidelines (*IPCC*, 2006)). Specifically, $N_2O$ is produced by microbial processes of nitrification and denitrification taking place on the deposition site (direct emissions), and leaching processes (indirect emissions).

Cultivation of organic soils: The FAOSTAT domain "Cultivation of organic soils" contains estimates of direct $N_2O$ emissions associated with the drainage of organic soils – histosols – under cropland and grazed grassland.

Burning-savanna: $N_2O$ emissions from the burning of vegetation biomass in the land cover types: Savanna, Woody Savanna, Open Shrublands, Closed Shrublands, and Grasslands. Burning-crop residues: $N_2O$ produced by the combustion of a percentage of crop residues burnt on-site. Burning-biomass: $N_2O$ emissions from the burning of vegetation biomass in the land cover types: Humid tropical forests, other forests, and organic soils.

## SI-3 The EDGAR v7.0 inventory

The new online version, EDGAR v7.0 (https://edgar.jrc.ec.europa.eu/dataset_ghg70) incorporates a full differentiation of emission processes with technology-specific emission factors and additional end-of-pipe abatement measures and as such updates and refines the emission estimates. The emissions are modelled based on the latest scientific knowledge and available global statistics primarily from International Energy Agency (*IEA*, 2021) for energy related sectors, FAO statistics (*FAO*, 2022) for agriculture, which were complemented for the rest of sectors with United States Geological Survey (USGS), International Fertiliser Association (IFA), Gas Flaring Reduction Partnership (GGFR)/U.S. National Oceanic and Atmospheric Administration (NOAA) and World Steel Association (worldsteel) recent statistics; the methods are those recommended by *IPCC* (2006). Official data submitted by the Annex I countries to the United Nations Framework Convention on Climate Change (UNFCCC) and to the Kyoto Protocol are used to some extent, particularly regarding control measures implemented since 1990 that are not described by international statistics. A fast-Track approach was used to extend the $N_2O$ emission time series for the latest years up to 2021 (*Crippa et al.*, 2021; *Crippa et al.*, 2022).

The $N_2O$ emission factors for direct soil emissions of $N_2O$ from the use of synthetic fertilizers, from manure used as fertilizers, and from crop residues are taken from *IPCC* (2006), which updated the default IPCC emission factor in the IPCC Good Practice Guidance (2000) with a 20% lower value. $N_2O$ emissions from the use of animal waste as fertilizer are estimated considering both the loss of N that occurs from manure management systems before manure is applied to soils and the additional N introduced by bedding material (*Janssens-Maenhout et al.*, 2019). $N_2O$ emissions from fertilizer use and $CO_2$ from urea fertilization are estimated based on IFA and FAO recent statistics.

$N_2O$ emissions from manure management are based on the distribution of manure management systems from Annex I countries reporting to the UNFCCC, *Zhou et al.* (2007) for China and *IPCC* (2006) for the rest of the countries.

Different $N_2O$ emission factors are applied to tropical and non-tropical regions. N and dry matter content of agricultural residues are estimated from the cultivation area and yield for 24 crop types from *FAO* (2022) and using emission factors of *IPCC* (2006).

Indirect $N_2O$ emissions from leaching and runoff of nitrate are estimated from N input to agricultural soils. Leaching and runoff are assumed to occur in all agricultural areas except non-irrigated dryland regions, which are identified with maps of FAO Geonetwork (https://www.fao.org/land-water/databases-and-software/geonetwork/en/). The fraction of N lost through leaching and runoff is based on the study of *Van Drecht et al.* (2003). The updated emission factor for indirect $N_2O$ emissions from N leaching and run-off from the *IPCC* (2006) guidelines is selected, while noting that it is 70% lower than the mean value of the 1996 IPCC Guidelines and the IPCC Good Practice Guidance *IPCC* (1996; 2000).

Indirect $N_2O$ emissions from atmospheric deposition of N of $NO_x$ and $NH_3$ emissions from non-agricultural sources, mainly fossil fuel combustion, are estimated using N in $NO_x$ and $NH_3$ emissions from these sources as activity data, based on EDGAR v7.0 database for these gases. The same emission factor from *IPCC* (2006) is used for indirect $N_2O$ from atmospheric deposition of N from $NH_3$ and NOx emissions, as for agricultural emissions (*Janssens-Maenhout et al.*, 2019).

The uncertainties for EDGAR $N_2O$ emissions estimated by *Solazzo et al.* (2021) are based primarily on the uncertainties in emissions factors and activity data statistics from the *IPCC* (2006). Globally, these emissions are accurate within an interval of ±113 for energy, -12% to +16% for industrial processes and product use, -225 to +302 for agriculture, -159% to 203% for waste and ±112% for others; the most uncertain emissions are those related to $N_2O$ from waste and agriculture.

## SI-4 The UNFCCC inventory (need description of UNFCCC)

The UNFCCC collects detailed data on GHG emissions from its parties. Following extensive guidance developed by IPCC (*Buendia et al.*, 2019; *Eggleston et al.*, 2006), parties to the convention prepare national GHG inventories, including emissions (and sinks) of $N_2O$. All anthropogenic activities are covered, in agriculture both direct and indirect $N_2O$ emissions are included. While IPCC basically provides emission factor approaches, parties are encouraged to take account of national specificities, use national factors and data, wherever available, or develop emission models, with adequate scientific proof provided. Combustion-related emissions and emissions from industrial processes may take advantage of emission monitoring or specific plant operation conditions, if provided. Emission processes that are not associated with anthropogenic activities are also not covered in the inventories.

Obligations and quality of data provided differ strongly by country category. High scrutiny is put on GHG inventories from countries listed in Annex-I of the convention (Annex-I countries include most European countries, U.S. and Canada, Australia and New Zealand, and Japan). Annex-I countries are obliged to provide annual national inventories in considerable detail and have to be very transparent also in terms of methodology used and underlying information. Each year, time-series of emissions and underlying data since 1990 (in a few cases, alternative base years are used) up to the pre-previous year are freshly provided in April each year (e.g., in April 2023 data up to the year 2021 had to be provided), leading to a homogeneous data series. Reports and emission data are provided (to UNFCCC, and to all users from the UNFCCC web site at https://unfccc.int/reports) in standardized format such that they can be transferred to databases. National results are routinely being checked and evaluated by expert teams in form of specific internal and external audits to assure data quality and consistency.

National information is highly relevant also for non-Annex I countries to the UNFCCC and is being collected and distributed by UNFCCC as well. Requirements are much less stringent, however, as parties are expected to provide data only according to their own capabilities and the support they get from other countries. The so-called Biannual Update Reports are to be prepared every other year only. While in principle following the same IPCC guidance, commitments to format, timing, and quality assessment are by far less stringent, and the own ambition level of the respective party (country) may determine much of the outcome. In any case, self-reporting of a country always also means the party is willing to take the responsibility of the emissions reported.

The “EDGAR/UNFCCC” dataset used in this paper utilizes the database for Annex-1 countries for emissions from fossil-fuel consumption, industrial processes, waste and wastewater, and merges with the respective set derived from EDGARv7.0 for all remaining countries.

**SI-5 The SRNM model:** Flux upscaling model

The SRNM model (Wang et al., 2020) was applied to simulate direct cropland-$N_2O$ emissions. In SRNM, $N_2O$ emissions were simulated from N application rates using a quadratic relationship, with spatially variable model parameters that depend on climate, soil properties, and management practices. The original version of SRNM was calibrated using field observations only from China (Zhou et al., 2015). In this study, we used the global $N_2O$ observation dataset to train it to create maps of gridded annual emission factors of $N_2O$ and the associated emissions at 5-minute resolution from 1901 to 2014(Cui et al., 2021). The gridded EF and associated direct cropland-$N_2O$ emissions are simulated based on the following equation:

$$E_{ijt} = \alpha_{ij} N_{ijt}^2 + \beta_{ij} N_{ijt} + \varepsilon_{ijt}, \ \forall i \tag{21}$$

where

$$\alpha_{ij} \sim N\left( \sum_k \left( x_k \lambda_{ijk} \right), \sigma_{ijk}^2 \right), \ \beta_{ij} \sim N\left( \sum_k \left( x_k \phi_{ijk} \right), \sigma_{ijk}'^2 \right) \tag{22}$$

$$\lambda_{ijk} \sim N\left( \mu_{ijk}, \omega_{ijk}^2 \right), \ \phi_{ijk} \sim N\left( \mu_{ijk}', \omega_{ijk}'^2 \right), \ \varepsilon_{ijt} \sim N\left( 0, \tau^2 \right) \tag{23}$$

and $i$ denotes the sub-function of $N_2O$ emission ($i$=1, 2, …, $I$) that applies for a sub-domain division $W_i$ of six climate or soil factors, $j$ represents the type of crop ($j$=1-2, 1 for upland crops and 2 for paddy rice), $k$ is the index of climate or soil factors ($k$=1-6, i.e., soil pH, clay content, SOC, BD, the sum of cumulative precipitation and irrigation, mean daily air temperature). $W_i$ denotes a set of the range of multiple $x_k$. $E_{ijt}$ denotes direct $N_2O$ emission flux (kg N ha$^{-1}$ yr$^{-1}$) estimated for crop type $j$ in year $t$ in the $i$th sub-domain, $N_{ijt}$ is N application rate (kg N ha$^{-1}$ yr$^{-1}$), and $a_{ij}$ and

$bij$ are defined as summation of the product of $x_k$ and $l_{ijk}$ over $k$. The random terms $l$ and $f$ are assumed to be independent and normally distributed, representing the sensitivity of $a$ and $b$ to $x_k$. $e$ is the model error. $m$ and $m¢$ are the mean effect of $x_k$ for $a$ and $b$, respectively. $s$, $s¢$, $w$, $w¢$, and$t$ are standard deviations. Optimal sub-domain division, associated parameters mean values and standard deviations were determined by using the Bayesian Recursive Regression Tree version 2 (BRRT v2), constrained by the extended global cropland-$N_2O$ observation dataset. The detailed methodological approach of the BRRT v2 is described by Zhou et al (2015).

**Global cropland $N_2O$ observation dataset**

We aggregated cropland $N_2O$ flux observation data from 180 globally distributed observation sites from online databases, on-going observation networks, and peer-reviewed publications (Figure SI-1). Chamber-based observations were only included in this dataset. These data repositories are as follows: the NitroEurope, CarbonEurope, GHG-Europe (EU-FP7), GRACEnet, TRAGnet, NANORP, and 14 meta-analysis datasets (*Decock*, 2014; *Harris et al.*, 2014; *Helgason et al.*, 2005; *Hénault et al.*, 2005; *Hickman et al.*, 2014; *Kim et al.*, 2013a; *Kim et al.*, 2013b; *Lehuger et al.*, 2011; *Leppelt et al.*, 2014; *Rochette and Janzen*, 2005; *Sacks et al.*, 2010; *Shcherbak et al.*, 2014; *Stehfest and Bouwman*, 2006; *Walter et al.*, 2015). Four types of data were excluded from our analysis: (i) observations without a zero-N control for background $N_2O$ emission, (ii) observations from sites that used controlled-release fertilizers or nitrification inhibitors, (iii) observations not covering the entire crop growing season, (iv) observations made in laboratory or greenhouse. We then calculated cropland-$N_2O$ emissions as the difference between observed $N_2O$ emission (E) and background $N_2O$ emission ($E_0$). Values of EF were estimated for each nonzero N application rate ($N_a$) as direct cropland-$N_2O$ emission divided by $N_a$: $\mathrm{EF} = (\mathrm{E} - \mathrm{E}_0)/N_a$. This yielded a global dataset of direct cropland-$N_2O$ emissions, N-rate-dependent $N_2O$ EFs and fertilization records from each site (i.e., 1,052 estimates for upland crops from 152 sites and 154 estimates for paddy rice from 28 sites), along with site-level information on climate, soils, crop type, and relevant experimental parameters. Total numbers of sites and total measurements in the dataset were more than doubled those for previous datasets of $N_2O$ EF. The extended global $N_2O$ observation network covered most of fertilized croplands, representing a wide range of environmental conditions globally. For each site in our dataset, the variables included four broad categories: $N_2O$ emissions data, climate data (cumulative precipitation and mean daily air temperature), soil attributes (soil pH, clay content, SOC, BD), and management-related or experimental parameters (N application rate, crop type). More details on global cropland $N_2O$ observation dataset can be found in *Cui et al.* (2021).

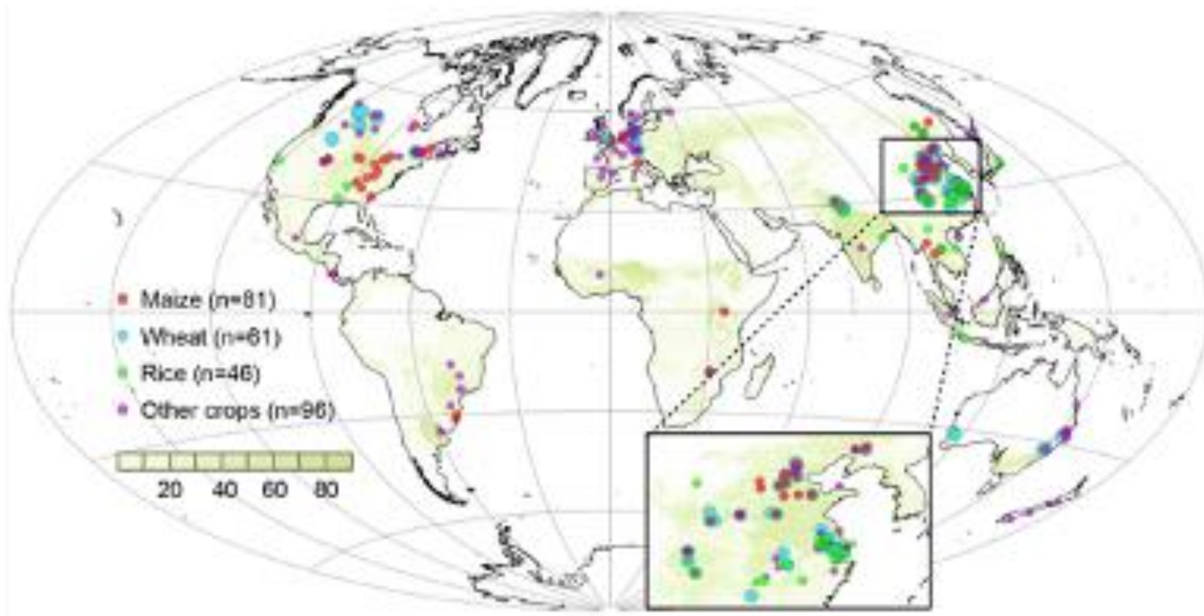


**Figure SI-1 Global observation dataset of $N_2O$ EF for direct soil emissions.** Green area indicates the harvested areas of all crops derived from the Earthstat. Sites are indicated in different colors for maize, wheat, rice, and other crops.

**Gridded input datasets**:

The updated SRNM model was driven by many input datasets, including climate, soil properties, agricultural management practices (e.g., fertilization, tillage, irrigation), as well as the historical distribution of cropland. Cumulative precipitation and mean daily air temperature over the growing season were acquired from the CRU TS V4.06 climate dataset (0.5-degree resolution) (*Harris et al.*, 2014), where growing season in each grid cell was identified following *Sacks et al.* (2010)The patterns of SOC, clay content, BD, and soil pH were acquired from the HWSD v1.2 ((*Berdanier and Conant*, 2012), 1-km resolution). Both climate and soil properties were re-gridded at 5-arc-minute spatial resolution using a first-order conservative interpolation widely used in the CMIP5 model intercomparison (*Yang et al.*, 2017). The annual cropland area at 5-arc-minute spatial resolution from 1961 to 2020 was obtained from the History Database of the Global Environment (HYDE 3.2.1) (*Goldewijk et al.*, 2017).

For fertilization, crop-specific N fertilizer inputs (including synthetic N fertilizers, crop residues and manure), fertilizer types, and placement during 1961-2020 were obtained from Adalibieke et al., (2023). The frequency (i.e., one or multiple times) of N fertilization were the same as *Cui et al.* (2021) and we assumed that the frequency remained constant during the study period. For tillage, the fraction of tillage by crop during 1961-2020 was obtained from Adalibieke et al., (2023), which was constructed with the country and province (or state) level no-tillage area data during 1961-2020 and downscaled to grid with the method of *Porwollik et al.* (2019). For irrigation, the History Database of the Global Environment (HYDE version 3.2) (*Goldewijk et al.*, 2017) and the MIRCA2000 dataset (*Portmann et al.*, 2010) were used to compile the global crop-specific irrigation proportion data from year 1961 to 2020. Categories of cropland in HYDE provided new distinctions with irrigated and rain-fed crops (upland crops, other than rice), irrigated and rain-fed rice during 1960-2017. The national-level dataset of "Agricultural area actually irrigated" was obtained from (*FAO*, 2022), which was used to scale the baseline year 2015 maps of irrigated area from HYDE over the period 2016-2020. The area of irrigated upland crops from HYDE was first disaggregated into 21 crops based on the irrigated proportion from MIRCA2000 for per grid cell. We assumed an even share of irrigated area by each upland crop during the period 1961-2020, like MIRCA2000. Finally, the crop-specific irrigated area was masked by reporting harvested area, then the irrigated proportion of each crop can be calculated as the crop-specific irrigated area divided by the physical area of each crop. For rice, we further divided irrigated rice into continuously and intermittently flooded systems as provided by *Cui et al.* (2021), and we assumed that the irrigation proportion was kept the same during the study period.

## SI-6 Global N flow in aquaculture

We applied the IMAGE-GNM aquaculture nutrient budget model for shellfish and finfish (*Bouwman et al.*, 2013; *Bouwman et al.*, 2011) to calculate the nutrient flows in aquaculture production systems. These flows comprise feed inputs, retention in the fish, and nutrient excretion. Individual species within crustaceans, seaweed, fish and molluscs are aggregated to the International Standard Statistical Classification of Aquatic Animals and Plants (ISSCAAP) groups (*FAO*, 2022), for which production characteristics are specified. Feed and nutrient conversion rates are used for each ISSCAAP group to calculate the feed and nutrient intake based on production data from FAO (*FAO*, 2020). Feed types include home-made aquafeeds and commercial compound feeds with different feed conversion ratios that also vary in time due to efficiency improvement; in addition, the model accounts for algae in ponds, that are often fertilized with commercial fertilizers or animal manure, consumed by omnivore fish species like carp. A special case is the filter-feeding bivalves that filter seston from the water column, and excrete pseudofeces, feces and dissolved nutrients. Based on production data and tissue/shell nutrient contents, the model computes the nutrient retention in the fish. Using apparent digestibility coefficients, the model calculates outflows in the form of feces (i.e., particulate nutrients) and dissolved nutrients. Finally, nutrient deposition in pond systems and recycling are calculated. For computing the $N_2O$ emissions, we consider the amount of N released to the environment, i.e., the difference between N intake and N in the harvested fish, which includes all the nutrient excretion. Since in pond cultures part of that N is managed, we made the amount of N recycling explicit, as well as ammonia emissions from ponds. This is to avoid double counting when computing $N_2O$ emissions from crop production.

## SI-7 Continental Shelves $N_2O$ fluxes

$N_2O$ emissions from the global ocean do not include the contribution from continental shelves and are added here using the extended mask of *Laruelle et al.* (2017) to delineate the coastal ocean. This mask excludes estuaries and inland water bodies, while its outer limit is set 300 km away from the shoreline. Within this coastal ocean domain, gridded $N_2O$ emissions were calculated using one data-driven estimate and three high-resolution model estimates from two distinct models, all interpolated on the same 0.25° x 0.25° grid. Models and data are each covering different time-periods and only one climatology is provided, keeping the original timespan of each product: 1988-2017 for the observation-based product that relied on a random-forest (RF) algorithm to interpolate $N_2O$ data (*Yang et al.*, 2020) from the MEMENTO database (MEM-RF) (*Kock and Bange*, 2015), 1998-2018 for the estimate relying on the high-resolution configuration (*Berthet et al.*, 2019) of the global ocean-biogeochemical component of CNRM-ESM2-1 (CNRM-0.25°), 1998-2013 and 2006-2013 for the estimates relying on the ECCO-Darwin model running at 1/3°

(ECCO-Darwin1) and 1/6° (ECCO-Darwin2), respectively. The resulting climatology can be considered as broadly representative of the last 2-3 decades. Each product is further described as follows:

**MEM-RF**

The $N_2O$ air-sea flux reconstruction by *Yang et al.* (2020) is based on a synthesis of over 158,000 observations of $N_2O$ mixing ratio, partial pressure, and concentration in the surface ocean from the MEMENTO database (https://memento.geomar.de) (*Kock and Bange*, 2015) and additional cruises (Dataset S1) (*Yang et al.*, 2020). $N_2O$ measurements are converted to surface $N_2O$ mixing ratio anomalies using observations from the NOAA atmospheric flask dataset (*Hall et al.*, 2007), and extrapolated to a 0.25-degree resolution global monthly climatology using an ensemble of 100 random forest realizations. The random forest algorithm predicts $N_2O$ mixing ratio anomalies based on their relationship to oceanographic predictors that include hydrographic variables, nutrients, oxygen, chlorophyll, net primary production, and seafloor depth. Reconstructed mixing ratio climatologies are used to estimate air-sea fluxes by applying a commonly used gas exchange parameterization (*Wanninkhof*, 2014). Two formulations of piston velocity are adopted: one based on a quadratic dependence on wind speed (*Wanninkhof*, 2014), and one that explicitly accounts for bubble-mediated fluxes (*Liang et al.*, 2013). Sea ice cover, surface temperature, salinity and atmospheric pressure are taken from ERA5 reanalysis (*Hersbach et al.*, 2017). Calculations are performed with two high-resolution wind products (ERA5 and CCMP) that are available at 0.25, 6-hourly resolution for the period from 1988 to 2017, yielding four permutations of the piston velocity. The resulting ensemble of 400 global $N_2O$ air–sea flux estimates is averaged in time to obtain monthly mean climatologies. A description of the dataset and methods is presented in *Yang et al.* (2020). The code used to produce these datasets is archived on a public GitHub repository at https://github.com/yangsi7/mapping-ocean-n2o (DOI: 10.5281/zenodo.3757194).

**CNRM-0.25°**

$N_2O$ fluxes have been inferred from the global ocean-biogeochemical component of CNRM-ESM2-1 (*Séférian et al.*, 2019) run at 0.25° horizontal resolution with 75 vertical levels in the ocean. This high-resolution configuration is described in *Berthet et al.* (2019) and is based on the NEMOv3.6 oceanic model (*Madec*, 2008), the multi-category sea ice model GELATOv6 (*Salas y Mélia*, 2002) and the PISCESv2-gas model for marine biogeochemistry (*Aumont et al.*, 2015), which includes an updated version of (*Martinez-Rey et al.*, 2015) for the marine $N_2O$ module. The simulation was first spun-up during 300 years under preindustrial conditions and then has been forced by the OMIP2-compliant JRA55-do-1-5 atmospheric reanalysis (*Tsujino et al.*, 2020; *Tsujino et al.*, 2018) considering the historical evolution of $CO_2$ and $N_2O$ in the atmosphere since the year 1850. Boundary conditions for nitrogen deposition and riverine inputs are prescribed from monthly climatologies. The suboxic production of $N_2O$ uses the oxygen-dependent formulation of *Jin and Gruber* (2003) and is enhanced at low oxygen concentrations. This formulation encompasses $N_2O$ production during remineralization, nitrification and grazing, as well as a sink term corresponding to $N_2O$ consumption under anoxic conditions by denitrification. The oceanic $N_2O$ partial pressure is computed based on the surface $N_2O$ concentration and the $N_2O$ solubility in the ocean. Sea-to-air $N_2O$ fluxes are then computed using the standard gas exchange parameterization of *Wanninkhof* (1992; 2014).

**ECCO-Darwin & ECCO2-Darwin**

To generate global air-sea fluxes of nitrous oxide ($N_2O$) from the global ocean we have used the ECCO-Darwin Model (*Carroll et al.*, 2020). The ECCO-Darwin model is based on MITgcm and it has a nominal horizontal resolution of 1/3 of a degree with 50 vertical levels where in the top 100 meters the model is vertically resolved with 10-meter grid boxes. The ECCO-Darwin model is forced with an atmospheric forcing corresponding to the 1992-present optimized with adjoint technique in order to realistically represent the observed physical climate phenomena such as El Nino, the Pacific Decadal Oscillation, the North Pacific "Warm Blob", etc. A more detailed description of the model forcing and the Darwin biogeochemical model configuration used in this study can be found in *Carroll et al.* (2020).

The Darwin biogeochemical/ecological model (*Carroll et al.*, 2020; *Manizza et al.*, 2019) used for this study carries 33 biogeochemical tracers to explicitly represent the cycle of carbon, oxygen, phosphorus, silica, and iron in the global ocean. For this particular version of the model, we implemented a parameterization of the oceanic cycle of $N_2O$ using the scheme of *Nevison et al.* (2003)based on the oceanic oxygen cycle previously represented in ECCO2-Darwin model (*Ganesan et al.*, 2020). The air-sea gas flux of $N_2O$ was parameterized according to *Wanninkhof* (1992). In addition, a thermal- only $N_2O$ tracer (a tracer in which biogeochemical sources and sinks are suppressed but with the same solubility as $N_2O$) was also added to the model to isolate the process of ocean ventilation affecting the $N_2O$ concentration in the ocean at seasonal time scales as done in *Manizza et al.* (2012). The ECCO-Darwin numerical simulation was run for the 1992-2014 period, but we discarded the inclusion of the output relative to the 1992-1996 period in our analysis due to the model adjustment in this initial part of our numerical simulation.

## SI-8 Open Ocean $N_2O$ fluxes

$N_2O$ is produced in the open ocean by microbial activity during organic matter cycling in the subsurface ocean, and its production pathways are influenced by the local environmental oxygen level. In the oxic ocean $N_2O$ is produced as a byproduct during the oxidation of ammonia to nitrate, mediated by ammonia oxidizing bacteria and archaea. $N_2O$ is also produced and consumed in sub-oxic and anoxic waters through the action of marine denitrifiers during the multi-step reduction of nitrate to gaseous N. The oceanic $N_2O$ distribution therefore displays significant heterogeneity with background levels of 10-20 nmol/l in the well-oxygenated ocean basins, high concentrations (> 40 nmol/l) in hypoxic waters, and $N_2O$ depletion in the core of ocean oxygen minimum zones (OMZs).

For this synthesis open ocean $N_2O$ emissions to the atmosphere were compiled from four global ocean biogeochemistry models/Earth System models that simulate the production, consumption and circulation of oceanic $N_2O$ (Table 6). $N_2O$ flux exchange between ocean and atmosphere is derived using gas-exchange parameterizations applied to modeled surface ocean $N_2O$. Versions of the four submitting models also participated in the previous $N_2O$ budget synthesis (*Tian et al.*, 2020a). Model details and updates to the previous $N_2O$ budget synthesis are summarized below.
The models differ in aspects of physical configuration (e.g., spatial resolution), meteorological forcing applied at the ocean surface, and in their parameterizations of ocean biogeochemistry; specific details on individual models are provided in the publications listed in Table 1. Towards this $N_2O$ budget synthesis, modelling groups reported grid-resolved ($1^o \times 1^o$ horizontal resolution) monthly estimates of ocean-atmosphere $N_2O$ fluxes for the period 1980-2020 (or for as many years as possible in that period).

**U. Bern: Bern-3D**

$N_2O$ fluxes are derived from the Bern-3D Earth System Model of Intermediate Complexity which includes a prognostic marine biogeochemistry model (based on (*Parekh et al.*, 2008) and (*Tschumi et al.*, 2011)). Configuration of the model for simulation of $N_2O$ is outlined in *Battaglia and Joos* (2018). Model simulations were run at a native resolution of horizontal resolution of 41 by 40 grid cells and 32 logarithmically scaled vertical layers. Modifications of the biogeochemistry model relevant for the $N_2O$ cycle include the assignment of organic matter remineralization to aerobic and anaerobic pathways dependent on mean grid-cell dissolved oxygen level. $N_2O$ is produced by nitrification as a product of remineralization rate and a specified $N_2O$ yield which has a functional form dependent on oxygen level (see details in (*Battaglia and Joos*, 2018)). $N_2O$ consumption by denitrification processes is represented by a first-order kinetics formulation which also includes a dependence on local oxygen level to account for the relative importance of denitrification-related $N_2O$ production and consumption processes in each gridcell. Measurements of dissolved $N_2O$ (surface and interior) from the MEMENTO database (*Kock and Bange*, 2015) together with an ensemble of model runs are used to constrain the model parameters governing $N_2O$ production and consumption mechanisms. From a pre-industrial equilibrium state the model is forced by historical CO2 emissions, non-CO2 radiative forcing, and land-use changes. $N_2O$ in the atmosphere is prescribed based on historical data.

**CNRM: CNRM-ESM2-1**

$N_2O$ fluxes are provided by the CNRM-ESM2-1 Earth System model. The ocean model component is based on NEMO Version 3.6 (*Madec et al.*, 2017) and coupled to the GELATO sea ice model (*Salas y Mélia*, 2002) Version 6 and the marine biogeochemical model PISCESv2-gas (*Aumont et al.*, 2015). The spatial model resolution follows the eORCA1L75 grid, with a nominal horizontal resolution of 1° and with higher resolution in the tropics (increasing to ~(1/3)°). The model has 75 vertical levels with higher resolution towards the ocean surface. The simulations were forced at the surface by the atmospheric state of JRA55-do v1.5.0 (*Tsujino et al.*, 2018). Atmospheric N2O concentration is given as annual means as specified by CMIP6 protocols and is linearly interpolated in time. Parameterization of the marine $N_2O$ cycle follows that of *Martinez-Rey et al.* (2015) with some modifications. $N_2O$ production is driven by an oxygen-dependent yield of $N_2O$, which encompasses production from denitrification and nitrification processes. This formulation also assumes a constant background yield representing $N_2O$ production by nitrification and a consumption of $N_2O$ in suboxic conditions. Originally implemented by *Martinez-Rey et al.* (2015), the marine $N_2O$ parameterization has benefited from a recoding and an improved calibration presented in *Berthet et al.* (2023). Further details of the model biogeochemistry and configuration are provided by *Séférian et al.* (2019) and *Berthet et al.* (2019).

**UVic2.9**

$N_2O$ model fluxes are derived from the UVic2.9, Earth System Model of Intermediate Complexity with prescribed monthly climatological winds (*Kalnay et al.*, 1996) and ice sheets (*Peltier*, 2004), configuration outlined in *Landolfi et al.* (2017). Oceanic subsurface $N_2O$ production is parameterized following (*Zamora and Oschlies*, 2014), as a function of $O_2$ consumption with a linear $O_2$ dependency, inherently including both nitrification and denitrification. In $O_2$-deficient waters (<4 mmol $m^{-3}$), denitrification becomes a sink of $N_2O$ consumed at a constant rate. The gradient driving the air-sea $N_2O$ gas exchange, is computed online based on departure of the surface ocean concentration from the saturation value using the solubility coefficients of *Weiss and Price* (1980) and time-varying prescribed atmospheric $N_2O$ concentrations (historical and RCP8.5). The model was spun-up for 6000 years with preindustrial boundary conditions (solar and volcanic and aerosol forcing, fixed atmospheric $CO_2$ of 280 ppm and $N_2O$ of 276 ppb, and preindustrial atmospheric N deposition).

**UEA: NEMO-PlankTOM10.2**

$N_2O$ model fluxes are derived from the NEMO-PlankTOM10.2 ocean model. The physical circulation component is NEMO v3.1 (*Madec*, 2008), with horizontal resolution of 2$^o$ longitude, and a variable latitudinal resolution (average ~1$^o$) with higher resolution in the tropics and polar regions. The model has 30 vertical layers, with variable resolution ranging from 10m in the upper 100m to 500m at depths of 5000 m. The biogeochemical component relies on the marine ecosystem model PlankTOM10, which includes representation of 10 plankton functional types (*Le Quéré et al.*, 2016). It has been extended by *Buitenhuis et al.* (2018) to include nitrogen cycle processes, and prognostic and diagnostic models of $N_2O$ production. $N_2O$ is produced from nitrification and denitrification pathways, with oxygen dependent yields employed to account for varying production and consumption processes in hypoxic waters. Nitrogen cycle parameters are optimized using ocean databases of dissolved $N_2O$ (MEMENTO, *Kock and Bange* (2015)) nitrification rates (*Yool et al.*, 2007), and surface ammonium concentrations (*Johnson et al.*, 2015; *Paulot et al.*, 2015). Further details on model configuration are provided in (*Buitenhuis et al.*, 2018).

## SI-9 Net $N_2O$ emission from land cover change

This section mainly involves the calculation of post-deforestation $N_2O$ emissions, deforestation induced $N_2O$ reduction and $N_2O$ emissions from forest regrowth (afforestation or reforestation). The methods include both bookkeeping and process-based modeling.

### a. Deforestation area, crop/pasture expansion and secondary forests

The LUH2 v2h (land use harmonization, http://luh.umd.edu) land use data was used to derive the deforestation area and its partition between crops and pastures during 1860−2020. LUH2 categorizes forest lands into forested primary land and potentially forested secondary land, while croplands are divided into C3 annual crops, C3 perennial crops, C4 annual crops, C4 perennial crops, and C3 N-fixing crops.

In the empirical computation of deforestation induced $N_2O$ emissions, all sub-classes within each land use type were treated the same. Thus, only the annual transition area from forests to croplands or managed pasture was needed. In the process-based estimates, the DLEM model was improved to further account for the classifications of primary forests, secondary forests (further partitioned into established and newly converted by an age threshold of 15 years), croplands/pastures /rangelands (further partitioned into established and newly converted by an age threshold of seven nine years). Each land use type can be divided into several different plant functional types (PFTs). Specifically, within a grid cell, cropland can only be dominated by only one crop type. The pastures and rangelands can be either C3 type or C4 type. To generate the historical spatial distribution of PFTs, a potential vegetation map and the accompanied composition ratio map of each natural PFT acquired from the Synergetic Land Cover Product (SYNMAP) were jointly used with LUH2 v2h.

**b. Methods**

The bookkeeping method was mainly applied to the tropical areas, where forests generally have high $N_2O$ emissions. Specifically, the average tropical forest $N_2O$ emission rate of 1.974 kg $N_2O$-N ha-1 yr-1 was adopted as the baseline. Two logarithmic response curves of soil $N_2O$ emissions (normalized to the baseline) after deforestation were developed: $y = -0.31\ln(x) + 1.53$ and $y = -0.454\ln(x) + 2.21$. This form of the response functions can effectively reproduce the short-lived increase in soil $N_2O$ emissions after initial forest clearing and the gradually declining emission rates of converted crops/pastures (*Melillo et al.*, 2001; *Verchot et al.*, 1999). Using these two curves and the baseline, we kept track of the $N_2O$ reduction of tropical forests and the post-deforestation crop/pasture $N_2O$ emissions at an annual timescale.

There are not many studies on $N_2O$ emissions from secondary tropical forests that regrowth after crop or pasture abandonment. *Sullivan et al.* (2019) lumped together all forms of N "gas loss" including NO and $N_2O$ for secondary forests across the tropics and the results showed gas loss gradually increases with age since the regrowth of secondary forest. *Keller and Reiners* (1994) also reported a gradual recovery of soil nitrate and soil emissions of $N_2O$ and nitric oxide (NO) during 20 years of secondary forest succession, which however did not return to the level of the primary forests. In this study, using field observations from *Davidson et al.* (2007) and *Keller and Reiners* (1994), we regressed normalized $N_2O$ emissions (relative to a reference mature forest) of secondary tropical forests with their ages as $y$=0.0084$x$ + 0.2401 ($R^2$ = 0.44; unit of $x$ is year). The derived $y$ values were multiplied by tropical forest $N_2O$ emissions estimated by NMIP2 models that do not distinguish secondary forests from primary forests.

The DLEM model was run with varying climate and $CO_2$ with other factors held constant to estimate forest baseline emissions and unfertilized crop/pasture emissions from 1860-2020. The climate data were acquired from CRUJRA, which is a fusion of the CRU and JRA reanalysis products at a spatial resolution of 0.5° × 0.5° and a daily time-step. The atmospheric $CO_2$ data were obtained from NOAA GLOBLVIEW-CO2 dataset (https://www.esrl.noaa.gov), which are derived from atmospheric and ice core measurements. In the tropical area, both estimates from the DLEM model and the bookkeeping method were adopted, whereas in extra-tropical area, we only adopted the DLEM outputs.

**SI-10 Inland water, estuaries, and coastal vegetation**

**a. Dynamic Land Ecosystem Model-Terrestrial/Aquatic Continuum (DLEM-TAC)**

To quantify $N_2O$ emissions from global inland waters (rivers, lakes, and reservoirs), we use a process-based coupled terrestrial-aquatic model, which builds up on the Dynamic Land Ecosystem Model (DLEM). DLEM-TAC is a fully distributed, process-based land surface model which couples the major land processes (terrestrial hydrology, plant phenology and physiology, soil biogeochemistry) and aquatic dynamics (lateral transport and in-stream biogeochemistry) (*Pan et al.*, 2021; *Tian et al.*, 2015; *Tian et al.*, 2020b; *Yao et al.*, 2020). The land component of DLEM-TAC explicitly simulates the carbon, nitrogen, and water fluxes between plants, soil, and atmosphere, and the surface and drainage runoff and nitrogen load from the land module are used as input for the aquatic module. The simulated nitrogen load includes dissolved inorganic nitrogen (DIN), dissolved organic nitrogen (DON), particulate organic nitrogen (PON), and runoffs, sewers as the initial condition of the aquatic module.

DLEM-TAC aquatic module calculated lateral water transport and the associated aquatic biogeochemical processes by adopting a scale-adaptive scheme. The water transport scheme, which coupled hillslope flow, subnetwork flow, and main channel flow, simulated the water transport processes within grid cells. In the aquatic module, lakes and reservoirs were linked with small streams and large rivers, forming a river-lake-reservoir corridor (*Wollheim et al.*, 2008)). Particularly, lakes that are linked to small streams are typically small in size and are defined as small lakes, while those linked to large rivers are usually had large size and are defined as large lakes; similarly, reservoirs that are linked to main channels are considered as large reservoirs, while those that are linked to small streams are considered as small reservoirs. The incoming flow of a linked river-lake-reservoir corridor drains to lakes first, and the outflow rate of lakes and reservoirs is determined based on the predefined residence time obtained from the global lake dataset (*Lehner et al.*, 2011; *Messager et al.*, 2016; *Yao et al.*, 2022). The aquatic N module was developed based on the scale adaptive water transport scheme, including lateral transport, decomposition of organic matter, particle organic matter deposition, nitrification, and denitrification. The detailed description could be found in the previous studies (*Pan et al.*, 2021; *Tian et al.*, 2020b; *Yao et al.*, 2020).

Following our previous work referring to the development of water transport and biogeochemistry, we developed an inland water $N_2O$ module within the aquatic biogeochemical component of the DLEM framework (*Yao et al.*, 2020). The net fluxes of dissolved $N_2O$ (including physical and biogeochemical processes) in the main channel (high-order streams) and subnetwork (small rivers) are estimated as:

$$(\Delta M\_N2O) / \Delta t = Fa + Ywater + D - R - E \tag{20}$$

where M_N2O is the total mass of dissolved $N_2O$ in the main channel or subnetworks (g N), $\Delta t$ is the time step, Fa is advective $N_2O$ fluxes (g N $d^{-1}$), Ywater is the $N_2O$ production within the water column (g N $d^{-1}$), D is the dissolved $N_2O$ from rainfall to rivers (i.e. deposition) (g N $d^{-1}$) with an initial concentration equal to the atmospheric equilibrium $N_2O$ concentration, R is the flux from $N_2O$ reduction (g N $d^{-1}$) to nitrogen gas, and E is the riverine $N_2O$ efflux (g N $d^{-1}$) through the air-water interface.

Input data. The driving data of DLEM-TAC include the climate variables, atmospheric CO2 concentration, land use change, nitrogen (N) deposition, N fertilizer, and manure application with a spatial resolution of 0.5°× 0.5°. The daily climate variables (precipitation, mean temperature, maximum temperature, minimum temperature, and shortwave radiation) were obtained from the CRUNCEP dataset (https://vesg.ipsl.upmc.fr) for 1901-2019. Climate data of each year during 1850-1900 was randomly sampled from 1901-1920. Annual atmospheric CO2 concentration from 1900-2019 was obtained from the NOAA GLOBALVIEW-CO2 dataset (https://www.esrl.noaa.gov). The annual land use change data was derived from a potential natural vegetation map (synergetic land cover product) and a prescribed cropland area dataset from the history database of the global environment v.3.2 (HYDE 3.2, ftp://ftp.pbl.nl/hyde). The data of N fertilizer, manure N application, and N deposition data was obtained from (*Tian et al.*, 2022).

In the aquatic module, the required channel dataset included channel slope, channel width, and channel length generated from the Hydroshed dataset (*Lehner et al.*, 2008) and DDM30 dataset (*Döll and Lehner*, 2002). The flow direction and distance data were obtained from the Dominant River Tracing (DRT) dataset. For modeling water dynamics in lakes and reservoirs, we generated 0.5 grid level surface water area, upstream area, volume, depth, and average residence time for lakes based on the Hydrolakes dataset (*Messager et al.*, 2016), while the GRanD database provided the same information for reservoirs (*Lehner et al.*, 2011).

Simulation protocol. DLEM-TAC simulations include three steps: equilibrium run, spin-up run and two transit runs, one with dam operation close, and another one with dam operation open. First, the equilibrium run is required to obtain the initial and steady condition of carbon, nitrogen, and water pool at the pre-industrial level in each grid cell (*Thornton and Rosenbloom*, 2005). In this step, we held all the driving forces such as climate data, atmospheric $CO_2$ concentration, land use data, and nitrogen additions consistent with the first year's data we used in the simulation. Second, we conducted a 30-year spin-up run by randomly selecting climate data within the 1850s (*Tian et al.*, 2012a). This step can alleviate the disturbance of driving data changes in the transit run. Then we conduct the natural flow simulation with the dam model temporarily closed, and all the driving forces change over time. After the natural flow simulation, we set up a management flow simulation with the dam module open, specifically the dam module needs natural flow in the previous run as model input.

b**. Mechanistic Stochastic Modeling of $N_2O$ emissions from large rivers, lakes, reservoirs, and estuaries:**

To calculate the cascading loads of TN and TP delivered to each water body along the river–reservoir–estuary continuum, we spatially routed all reservoirs from the GRanD database (*Lehner et al.*, 2011), with river networks from Hydrosheds 15s (*Lehner et al.*, 2008) and, at latitudes above 50°N, Hydro1K (http://edc.usgs.gov/products/elevation/gtopo30/hydro/), which were in turn connected to estuaries as represented in the "Worldwide Typology of Nearshore Coastal Systems" of *Dürr et al.* (2011). In addition, the global database HydroLAKES (*Messager et al.*, 2016) was used to topologically connect 1.4 million lakes with a minimum surface area of 0.1 $km^2$ within the river network. Note that besides natural lakes, HydroLAKES includes updated information on 6,796 reservoirs from the GRanD database, which was used in the study of *Maavara et al.* (2019). In order to estimate the TN and TP loads to each water body, we then relied on a spatially explicit representation of TN and TP mobilization from the watershed into the river network (see (*Maavara et al.*, 2019) for details (*Bouwman et al.*, 2009; *Van Drecht et al.*, 2009).

For the estimation of $N_2O$ emission, we applied two distinct model configurations, respectively named DS1 and DS2 in *Maavara et al.* (2019). DS1 estimates $N_2O$ emissions from denitrification and nitrification based on an EF of 0.9%, which is in the mean of published values (*Beaulieu et al.*, 2011), and the assumption that $N_2O$ production equals $N_2O$ emissions (*Maavara et al.*, 2019). For DS2, the reduction of $N_2O$ to $N_2$ during denitrification if $N_2O$ is not evading sufficiently rapidly from the water body is considered. The fluxes in the model represent lumped sediment-water column rates and were resolved at the annual timescale. The use of water residence time as an independent variable in both the mechanistic model and the upscaling process introduces an important kinetic refinement to existing global $N_2O$ emission estimates. Rather than applying an average EF (directly scaling $N_2O$ emissions to N inputs) to all water bodies, the use of water residence time explicitly adjusts for the extent of $N_2O$ production and emission that is kinetically possible within the timeframe available in a given water body. Simulated $N_2O$ emission rates were evaluated against UNFCCC measurement-based upscaling methods applied to reservoirs (*Deemer et al.*, 2016) and rivers (*Hu et al.*, 2016) as well as a UNFCCC observation-driven regional estimate of lake $N_2O$ emissions based on literature data (*Lauerwald et al.*, 2019).

**c. Meta analysis-based $N_2O$ emissions from large rivers**

Data from 70 published studies between 1998 and 2016 that provided $N_2O$ emission from streams and rivers were compiled by *Hu et al.* (2016). The $N_2O$ emission factors (EF = $N_2O$ /DIN) and emission rates (ER = EF * DIN load, kg $N_2O$-N $yr^{-1}$) were calculated for each studied river. Exploratory multiple regression analyses were conducted to predict EF and ER using various combinations of factors (N concentrations, loads, yields, DOC: DIN, discharge, and watershed area) and different functions. Among them, DIN yield (kg N $yr^{-1}$ $km^{-2}$) was identified as the best predictor of EF and ER. Using the optimal model and DIN loads for 6400 global rivers calculated by the NEWS2-DIN-S model (*McCrackin et al.*, 2014), we estimated global riverine $N_2O$ emissions (*Hu et al.*, 2016).

**d. Stream and river $N_2O$ emissions combining machine-learning and model-based upscaling**

*Marzadri et al.* (2021) developed a novel approach that combines a data-driven Random Forest Machine Learning (RM-ML) model with a physically-based upscaling model to predict near global (neglecting Arctic and Antarctic areas) riverine $N_2O$ emissions flux ($F^*N_2O$ given by the ratio between the flux of $N_2O$, $FN_2O$, and the in-stream flux of dissolved inorganic nitrogen species FDIN) from both surface (i.e. water column) and subsurface (i.e. benthic zone and hyporheic zone) riverine environments. In particular, to capture the local scale processes responsible for $N_2O$ emissions and to provide estimations at different spatial scales (from local reach up to the global scale) the model compute two different denitrification Damköhler numbers (given by the ratio between a characteristics time of transport and a characteristics time of denitrification (*Marzadri et al.*, 2021; *Marzadri et al.*, 2017)) starting from the hydro-morphological and biogeochemical information provided by the RM-ML model. Model results at the local reach scale shows that nearly 50% of the riverine $N_2O$ emissions comes from small streams (i.e. widths lower than 10 m, although they represent only the 13% of the total riverine surface area worldwide) while at the large scale predict a near-global annual riverine $N_2O$ emissions around 72.8 $GgN_2O-N/yr$.

**e. Meta-analysis based $N_2O$ emissions from estuaries and coastal vegetation**

$N_2O$ emissions from estuaries and coastal vegetated ecosystems were obtained from a meta-analysis of observed $N_2O$ fluxes (*Rosentreter et al.*, 2023). In brief, the meta-data analysis relies on a categorization of estuaries into ‘tidal systems and deltas’, ‘lagoons’, and ‘fjords’. Water-air $N_2O$ fluxes from 123 estuary sites globally were then compiled from peer-reviewed publications until the end of 2020. Coastal vegetation comprises ‘mangrove’, ‘salt marsh’, and ‘seagrass’ ecosystems and $N_2O$ sediment-water-air fluxes were compiled from 55 sites globally from peer-reviewed publications until the end of 2020. A non-parametric bootstrapping method (1000 iterations of the median of samples) was used to resample $N_2O$ fluxes per unit area for each estuary and coastal vegetation type in each of the 18 regions using the 'boot' function in the package 'boot' in R software. Results from the bootstrapping output (minimum, Q1, median, mean, Q3, maximum) were then scaled to the surface area of each estuary and coastal vegetation type in each of the 18 RECCAP regions. If an ecosystem type had less than three sites in a region, we applied the global statistics of this type in this region. Note that the meta-data analysis only provides flux assessments at the scale of the 18 regions.

## SI-11 Atmospheric inversion models

Emissions were estimated using four independent atmospheric inversion frameworks (see Table 1). The frameworks all used a Bayesian inversion method. The approach used here finds the maximum posteriori (MAP), or optimal, estimate of emissions, that is, those, which when coupled to a model of atmospheric transport, provide the best agreement to observed $N_2O$ mixing ratios while being guided by their prior probability. In this particular case, where both the likelihood and prior probability are assumed to be distributed normally, the optimal emissions are equivalent to those that minimize the cost function,

$$J(\mathbf{x}) = \frac{1}{2}\left(\mathbf{x}-\mathbf{x_b}\right)^{\mathrm{T}}\mathbf{B}^{-1}\left(\mathbf{x}-\mathbf{x_b}\right)+\frac{1}{2}\left(\mathbf{y}-H(\mathbf{x})\right)^{\mathrm{T}}\mathbf{R}^{-1}\left(\mathbf{y}-H(\mathbf{x})\right) \tag{24}$$

where $\mathbf{x}$ and $\mathbf{x_b}$ are, respectively, vectors of the multivariate means of the posterior and prior emission distributions, $\mathbf{B}$ is the prior error covariance matrix for emissions, $\mathbf{y}$ is a vector of observed $N_2O$ mixing ratios, $\mathbf{R}$ is the observation error covariance matrix, and $H(\mathbf{x})$ is the model of atmospheric transport (for details on the inversion method see (*Tarantola*, 2005)). The optimal emissions, $\mathbf{x}$, were found by solving the first order derivative of equation (21):

$$J'(\mathbf{x}) = \mathbf{B}^{-1}\left(\mathbf{x}-\mathbf{x_b}\right)+\left(H'(\mathbf{x})\right)^{\mathrm{T}}\mathbf{R}^{-1}\left(\mathbf{y}-H(\mathbf{x})\right)=0 \tag{25}$$

where $(H'(\mathbf{x}))^{\mathrm{T}}$ is the sensitivity of the atmospheric observations to emissions, derived from an adjoint model of transport. In frameworks INVICAT, PyVAR-CAMS and GEOS-Chem, equation (5b) was solved using a variational approach (*Thompson et al.*, 2014; *Wells et al.*, 2015; *Wilson et al.*, 2014), which uses a descent algorithm and computations involving the forward and adjoint models. In framework MIROC4-ACTM (*Patra et al.*, 2018), equation (22) was solved directly by computing a transport operator, $\mathbf{H}$ from integrations of the forward model, such that $\mathbf{Hx}$ is equivalent to $H(\mathbf{x})$, and taking the transpose of $\mathbf{H}$ (*Patra et al.*, 2022).

Each of the inversion frameworks used a different model of atmospheric transport with different horizontal and vertical resolutions (see Table 1). The transport models TOMCAT and LMDz5, used in INVICAT and PyVAR-CAMS respectively, were driven by ECMWF ERA-5 and ERA-Interim wind fields respectively, MIROC4-ACTM was driven by JRA-55 wind fields, and GEOS-Chem was driven by MERRA-2 wind fields. While INVICAT, PyVAR-CAMS, and GEOS-Chem optimized the emissions at the spatial resolution of the transport model, MIROC4-ACTM optimized the error in the emissions aggregated into 84 land and ocean regions. All frameworks optimized the emissions with monthly temporal resolution. The transport models included an online calculation of the loss of $N_2O$ in the stratosphere due to photolysis and oxidation by $O(^1D)$ resulting in mean atmospheric lifetimes of between 118 and 129 years, broadly consistent with recent independent estimates of the lifetime of 116±9 yr (*Prather et al.*, 2015)).

All inversions used $N_2O$ measurements of discrete air samples from the National Oceanic and Atmospheric Administration Carbon Cycle Cooperative Global Air Sampling Network (NOAA). In addition, discrete measurements from the Commonwealth Scientific and Industrial Research Organisation network (CSIRO) as well as in-situ measurements from the Advanced Global Atmospheric Gases Experiment network (AGAGE), the NOAA CATS network, and from individual sites operated by University of Edinburgh (UE), National Institute for Environmental Studies (NIES), the Finnish Meteorological Institute (FMI) and the Japan Meteorological Agency (JMA) were included in INVICAT, PyVAR-CAMS and GEOS-Chem. Measurements from networks other than NOAA were corrected to the NOAA calibration scale, NOAA-2006A, using the results of the WMO Round Robin inter-comparison experiment (https://www.esrl.noaa.gov/gmd/ccgg/wmorr/), where available. For AGAGE and CSIRO, which did not participate in the WMO Round Robins, the data at sites where NOAA discrete samples are also collected were used to calculate a linear regression with NOAA data, which was applied to adjust the data to the NOAA-2006A scale. For the remaining CSIRO sites where there were no NOAA discrete samples, the mean regression coefficient and offset from all other CSIRO sites were used. The inversions used the discrete sample measurements without averaging, and hourly or daily means of the in-situ measurements, depending on the particular inversion framework.

Each framework applied its own method for calculating the observation space uncertainty, the square of which gives the diagonal elements of the observation error covariance matrix R. The observation space uncertainty accounts for measurement and model representation errors and is equal to the quadratic sum of these terms. Typical values for the observation space uncertainty were between 0.3 and 0.5 ppb for all inversion frameworks.

Prior mean emissions were based on estimates from terrestrial biosphere and ocean biogeochemistry models as well as from inventories. INVICAT, PyVAR-CAMS and GEOS-Chem used the same prior estimates for emissions from natural and agricultural soils from the model OCN v1.1 (*Zaehle et al.*, 2011) and for biomass burning emissions from GFEDv4.1s. For non-soil anthropogenic emissions (namely those from energy, industry and waste sectors), INVICAT, PyVAR-CAMS, and GEOS-Chem used EDGAR v5. MIROC4-ACTM used the VISIT model (*Inatomi et al.*, 2010; *Ito et al.*, 2018) for emissions from natural soils and EDGAR 4.2 for all anthropogenic emissions, including agricultural waste burning, but did not explicitly include a prior estimate for wildfire emissions.

For the prior mean estimate of ocean fluxes, INVICAT, PyVAR-CAMS and GEOS-Chem used the prognostic version of the PlankTOM-v10.2 model (*Buitenhuis et al.*, 2018) with a global total source 2.5 TgN $yr^{-1}$. Prior uncertainties were estimated in all the inversion frameworks for each grid cell (INVICAT, PyVAR-CAMS and GEOS-Chem) or for each region (MIROC4-ACTM) and the square of these uncertainties formed the diagonal elements of the prior error covariance matrix **B**. INVICAT, PyVAR-CAMS and GEOS-Chem estimated the uncertainty as proportional to the prior value in each grid cell, but MIROC4-ACTM set the uncertainty uniformly for land regions at 1 Tg N $yr^{-1}$ and for ocean regions at 0.5 Tg N $yr^{-1}$. INVICAT also included off-diagonal covariances in B corresponding to a spatial correlation between flux uncertainties of 500 km and assumed a semi-exponential distribution of uncertainties so as to restrict the possibility of negative fluxes.

## SI-12 Atmospheric $N_2O$ Observation Networks

The NOAA Network: For atmospheric $N_2O$ observations from the NOAA network (Dutton et al. 2023), we used global mean mixing ratios from the NOAA Global Monitoring Laboratory (GML) (combined dataset based on measurements from five different measurement programs [HATS old flask instrument, HATS current flask instrument (OTTO), the Carbon Cycle and Greenhouse Gases (CCGG) group Cooperative Global Air Sampling Network (https://www.esrl.noaa.gov/gmd/ccgg/flask.php), HATS in situ (RITS program), and HATS in situ (CATS program)]. CCGG provides uncertainties with each measurement (see site files: ftp://aftp.cmdl.noaa.gov/data/greenhouse_gases/n2o/flask/surface/). The CCGG measurements for $N_2O$ analysis from more than 50 sites globally was changed to tunable infrared laser direct absorption spectroscopy (TILDAS) in mid-2019 from gas chromatography. About 40 sites of them (mostly Marine Boundary Layer sites) are used to calculate CCGG monthly mean global $N_2O$ levels. Monthly mean observations from different NOAA measurement programs are statistically combined to create a long-term NOAA/ESRL GML dataset. Uncertainties (1 sigma) associated with monthly estimates of global mean $N_2O$, are ~1 ppb from 1977−1987, 0.6 ppb from 1988−1994, 0.3−0.4 ppb from 1995−2000, and 0.1 ppb from 2001-2017. NOAA data are generally more consistent after 1995, with standard deviations on the monthly mean mixing ratios at individual sites of ~0.5 ppb from 1995−1998, and 0.1−0.4 ppb after 1998. A detailed description of these measurement programs and the method to combine them are available via https://www.esrl.noaa.gov/gmd/hats/combined/N2O.html.
THE AGAGE network: The Advanced Global Atmospheric Gases Experiment (AGAGE) global network (and its predecessors ALE and GAGE) (Prinn et al., 2018) has made continuous high-frequency gas chromatographic (GC) measurements with electronic capture detection (ECD) of $N_2O$ at five globally distributed sites since 1978. Improved GC/ECD methods have been deployed over time resulting in $N_2O$ measurement precision of about 0.35% in ALE, 0.13% in GAGE (Prinn et al., 1990) and 0.05% in AGAGE (Prinn et al., 2008; 2018). We used the global mean of AGAGE $N_2O$ measurements during 1980−2020 which are reported on the Scripps Institution of Oceanography SIO-16 scale. Further information on AGAGE stations, instruments, calibration, uncertainties and access to data is available at the AGAGE Data website: https://www.osti.gov/dataexplorer/biblio/dataset/1841748.

The CSIRO network: The CSIRO flask network (Francey et al., 2003) consists of nine sampling sites distributed globally and has been in operation since 1992. Flask samples are collected approximately every two weeks and shipped back to CSIRO GASLAB for analysis. Samples were analyzed by gas chromatography with electron capture detection (GC-ECD). One Shimadzu gas chromatograph labelled "Shimadzu-1" (S1) has been used over the entire length of the record and the measurement precision for $N_2O$ from this instrument is about 0.1%. $N_2O$ data from the CSIRO global flask network are reported on the NOAA-2006A $N_2O$ scale and are archived at the World Data Centre for Greenhouse Gases (WDCGG: https://gaw.kishou.go.jp/). Nine sites from the CSIRO network were used to calculate the annual global $N_2O$ mole fractions. Smooth curve fits to the $N_2O$ data from each of these sites were calculated using the technique outlined in Thoning et al. (1989), using a short-term cut-off of 80 days. The smooth curve fit data were then placed on an evenly spaced latitude (5 degree) versus time (weekly) grid using the Kriging interpolation technique. Finally, the gridded data were used to calculate the global annual values.

## References:


Adalibieke, W., Cui X.Q., Cai H.W., You L.Z., and Zhou F.: Global crop-specific nitrogen fertilization dataset in 1961-2020, Scientific Data 10, 617, 2023, https://www.nature.com/articles/s41597-023-02526-z

Asaadi, A., and Arora, V. K.: Implementation of nitrogen cycle in the CLASSIC land model, *Biogeosciences*, *18*(2), 669-706, 2021.

Aumont, O., Éthé, C., Tagliabue, A., Bopp, L., and Gehlen, M.: PISCES-v2: an ocean biogeochemical model for carbon and ecosystem studies, *Geoscientific Model Development Discussions*, *8*(2), 1375-1509, 2015.

Battaglia, G., and Joos, F.: Marine N2O emissions from nitrification and denitrification constrained by modern observations and projected in multimillennial global warming simulations, *Global Biogeochemical Cycles*, *32*(1), 92-121, 2018.

Beaulieu, J. J., Tank, J. L., Hamilton, S. K., Wollheim, W. M., Hall Jr, R. O., Mulholland, P. J., Peterson, B. J., Ashkenas, L. R., Cooper, L. W., and Dahm, C. N. : Nitrous oxide emission from denitrification in stream and river networks, *Proceedings of the National Academy of Sciences*, *108*(1), 214-219, 2011.

Berdanier, A. B., and Conant, R. T.: Regionally differentiated estimates of cropland N2O emissions reduce uncertainty in global calculations, *Global Change Biology*, *18*(3), 928-935, 2012.

Berthet, S., Jouanno, J., Séférian, R., Gehlen, M., and Llovel, W.: How does the phytoplankton–light feedback affect the marine N2O inventory?, *Earth System Dynamics*, *14*(2), 399-412, 2023.

Berthet, S., Séférian, R., Bricaud, C., Chevallier, M., Voldoire, A., and Ethé, C.: Evaluation of an online grid-coarsening algorithm in a global eddy-admitting ocean biogeochemical model, *Journal of Advances in Modeling Earth Systems*, *11*(6), 1759-1783, 2019.

Bouwman, A. F., Beusen, A. H. W., and Billen, G. : Human alteration of the global nitrogen and phosphorus soil balances for the period 1970–2050, *Global Biogeochemical Cycles*, *23*(4), 2009.

Bouwman, A. F., Beusen, A. H. W., Overbeek, C. C., Bureau, D. P., Pawlowski, M., and Glibert, P. M.: Hindcasts and future projections of global inland and coastal nitrogen and phosphorus loads due to finfish aquaculture, *Reviews in Fisheries Science*, *21*(2), 112-156, 2013.

Bouwman, A. F., Pawłowski, M., Liu, C., Beusen, A. H. W., Shumway, S. E., Glibert, P. M., and Overbeek, C. C.: Global hindcasts and future projections of coastal nitrogen and phosphorus loads due to shellfish and seaweed aquaculture, *Reviews in Fisheries Science*, *19*(4), 331-357, 2011.

Buendia, E., Tanabe, K., Kranjc, A., Baasansuren, J., Fukuda, M., Ngarize, S., Osako, A., Pyrozhenko, Y., Shermanau, P., and Federici, S.: 2019 Refinement to the 2006 IPCC Guidelines for National Greenhouse Gas Inventories*Rep.*, 2019.

Buitenhuis, E. T., Suntharalingam, P., and Le Quéré, C.: Constraints on global oceanic emissions of N2O from observations and models, *Biogeosciences*, *15*(7), 2161-2175, 2018.

Carroll, D., Menemenlis, D., Adkins, J. F., Bowman, K. W., Brix, H., Dutkiewicz, S., Fenty, I., Gierach, M. M., Hill, C., and Jahn, O.: The ECCO-Darwin data-assimilative global ocean biogeochemistry model: Estimates of seasonal to multidecadal surface ocean pCO2 and air-sea CO2 flux, *Journal of Advances in Modeling Earth Systems*, *12*(10), e2019MS001888, 2020.

Chatskikh, D., Olesen, J. E., Berntsen, J., Regina, K., and Yamulki, S.: Simulation of effects of soils, climate and management on N2O emission from grasslands, *Biogeochemistry*, *76*, 395-419, 2005.

Crippa, M., Solazzo, E., Guizzardi, D., Monforti-Ferrario, F., Tubiello, F. N., and Leip, A.: Food systems are responsible for a third of global anthropogenic GHG emissions, *Nature Food*, *2*(3), 198-209, 2021.

Crippa, M., Solazzo, E., Guizzardi, D., Van Dingenen, R., and Leip, A.: Air pollutant emissions from global food systems are responsible for environmental impacts, crop losses and mortality, *Nature Food*, 1-15, 2022.

Cui, X., Zhou, F., Ciais, P., Davidson, E. A., Tubiello, F. N., Niu, X., Ju, X., Canadell, J. G., Bouwman, A. F., and Jackson, R. B.: Global mapping of crop-specific emission factors highlights hotspots of nitrous oxide mitigation, *Nature Food*, *2*(11), 886-893, 2021.

Davidson, E. A., de Carvalho, C. J. R., Figueira, A. M., Ishida, F. Y., Ometto, J. P. H. B., Nardoto, G. B., Sabá, R. T., Hayashi, S. N., Leal, E. C., and Vieira, I. C. G.: Recuperation of nitrogen cycling in Amazonian forests following agricultural abandonment, *Nature*, *447*(7147), 995-998, 2007.

Davidson, E. A., Keller, M., Erickson, H. E., Verchot, L. V., and Veldkamp, E.: Testing a conceptual model of soil emissions of nitrous and nitric oxides: using two functions based on soil nitrogen availability and soil water content, the hole-in-the-pipe model characterizes a large fraction of the observed variation of nitric oxide and nitrous oxide emissions from soils, *Bioscience*, *50*(8), 667-680, 2000.

Decock, C.: Mitigating nitrous oxide emissions from corn cropping systems in the midwestern US: Potential and data gaps, *Environmental Science & Technology*, *48*(8), 4247-4256, 2014.

Deemer, B. R., Harrison, J. A., Li, S., Beaulieu, J. J., DelSontro, T., Barros, N., Bezerra-Neto, J. F., Powers, S. M., Dos Santos, M. A., and Vonk, J. A.: Greenhouse gas emissions from reservoir water surfaces: a new global synthesis, *BioScience*, *66*(11), 949-964, 2016.

Del Grosso, S. J., Parton, W. J., Mosier, A. R., Ojima, D. S., Kulmala, A. E., and Phongpan, S.: General model for N2O and N2 gas emissions from soils due to dentrification, *Global biogeochemical cycles*, *14*(4), 1045-1060, 2000.

Döll, P., and Lehner, B.: Validation of a new global 30-min drainage direction map, *Journal of Hydrology*, *258*(1-4), 214-231, 2002.

Dürr, H. H., Laruelle, G. G., van Kempen, C. M., Slomp, C. P., Meybeck, M., and Middelkoop, H.: Worldwide typology of nearshore coastal systems: defining the estuarine filter of river inputs to the oceans, *Estuaries Coasts*, *34*, 441-458, 2011.

Eggleston, H. S., Buendia, L., Miwa, K., Ngara, T., and Tanabe, K. : 2006 IPCC guidelines for national greenhouse gas inventories, 2006.

FAO (2020), FAO Fisheries and Aquaculture - FishStatJ - Software for Fishery and Aquaculture Statistical Time Series. In: FAO Fisheries and Aquaculture Division [online]. Rome. [Cited 3 November 2021]. , edited.

FAO (2022), FAOSTAT Climate Change, Emissions, Emissions Totals, edited.

Ganesan, A. L., Manizza, M., Morgan, E. J., Harth, C. M., Kozlova, E., Lueker, T., Manning, A. J., Lunt, M. F., Mühle, J., and Lavric, J. V.: Marine nitrous oxide emissions from three Eastern Boundary Upwelling Systems inferred from atmospheric observations, *Geophysical Research Letters*, *47*(14), e2020GL087822, 2020.

Goldewijk, K. K., Beusen, A., Doelman, J., and Stehfest, E.: Anthropogenic land use estimates for the Holocene–HYDE 3.2, *Earth System Science Data*, *9*(2), 927-953, 2017.

Hall, B. D., Dutton, G. S., and Elkins, J. W.: The NOAA nitrous oxide standard scale for atmospheric observations, *Journal of Geophysical Research: Atmospheres*, *112*(D9), 2007.

Harris, I. P. D. J., Jones, P. D., Osborn, T. J., and Lister, D. H.: Updated high-resolution grids of monthly climatic observations–the CRU TS3. 10 Dataset, *International journal of climatology*, *34*(3), 623-642, 2014.

Heinen, M.: Simplified denitrification models: overview and properties, *Geoderma*, *133*(3-4), 444-463, 2006.

Helgason, B. L., Janzen, H. H., Chantigny, M. H., Drury, C. F., Ellert, B. H., Gregorich, E. G., Lemke, R. L., Pattey, E., Rochette, P., and Wagner-Riddle, C.: Toward improved coefficients for predicting direct N2O emissions from soil in Canadian agroecosystems, *Nutrient Cycling in Agroecosystems*, *72*, 87-99, 2005.

Hénault, C., Bizouard, F., Laville, P., Gabrielle, B., Nicoullaud, B., Germon, J. C., and Cellier, P.: Predicting in situ soil N2O emission using NOE algorithm and soil database, *Global Change Biology*, *11*(1), 115-127, 2005.

Hersbach, H., Bell, B., Berrisford, P., Hirahara, S., Horányi, A., Muñoz-Sabater, J., Nicolas, J., Peubey, C., Radu, R., and Schepers, D.: Complete ERA5 from 1979: Fifth generation of ECMWF atmospheric reanalyses of the global climate, *Copernicus Climate Change Service Data Store*, 2017.

Hickman, J. E., Scholes, R. J., Rosenstock, T. S., Garcia-Pando, C. P., and Nyamangara, J.: Assessing non-CO2 climate-forcing emissions and mitigation in sub-Saharan Africa, *Current Opinion in Environmental Sustainability*, *9*, 65-72, 2014.

Hu, M., Chen, D., and Dahlgren, R. A.: Modeling nitrous oxide emission from rivers: a global assessment, *Global Change Biology*, *22*(11), 3566-3582, 2016.

Huang, Y., and Gerber, S.: Global soil nitrous oxide emissions in a dynamic carbon-nitrogen model, *Biogeosciences*, *12*(21), 6405-6427, 2015.

Hurtt, G. C., Chini, L., Sahajpal, R., Frolking, S., Bodirsky, B. L., Calvin, K., Doelman, J. C., Fisk, J., Fujimori, S., and Klein Goldewijk, K.: Harmonization of global land use change and management for the period 850–2100 (LUH2) for CMIP6, *Geoscientific Model Development*, *13*(11), 5425-5464, 2020.

IEA: World Energy Outlook 2021*Rep.*, IEA, Paris, 2021.

Inatomi, M., Ito, A., Ishijima, K., and Murayama, S.: Greenhouse gas budget of a cool-temperate deciduous broad-leaved forest in Japan estimated using a process-based model, *Ecosystems*, *13*, 472-483, 2010.

IPCC: Revised 1996 IPCC Guidelines for National Greenhouse Gas Inventories, 1996.

IPCC: Good practice guidance and uncertainty management in national greenhouse gas inventories, 2000.

IPCC: IPCC Guidelines for National Greenhouse Gas Inventories*Rep.*, Hayama, Japan, 2006.

Ito, A., Nishina, K., Ishijima, K., Hashimoto, S., and Inatomi, M.: Emissions of nitrous oxide (N 2 O) from soil surfaces and their historical changes in East Asia: a model-based assessment, *Progress in Earth Planetary Science*, *5*, 1-13, 2018.

Janssens-Maenhout, G., Crippa, M., Guizzardi, D., Muntean, M., Schaaf, E., Dentener, F., Bergamaschi, P., Pagliari, V., Olivier, J. G., and Peters, J. A.: EDGAR v4. 3.2 Global Atlas of the three major greenhouse gas emissions for the period 1970–2012, *Earth System Science Data*, *11*(3), 959-1002, 2019.

Jin, X., and Gruber, N.: Offsetting the radiative benefit of ocean iron fertilization by enhancing N2O emissions, *Geophysical research letters*, *30*(24), 2003.

Johnson, D. J., Niedbalski, N. P., Ervin, J. S., and Patnaik, S. S.: Ammonium carbamate-based heat exchanger reactor as an endothermic heat sink for thermal management, *International Journal of Heat Mass Transfer*, *91*, 766-776, 2015.

Kalnay, E., Kanamitsu, M., Kistler, R., Collins, W., Deaven, D., Gandin, L., Iredell, M., Saha, S., White, G., and Woollen, J.: The NCEP/NCAR 40-year reanalysis project, *Bulletin of the American meteorological Society*, *77*(3), 437-472, 1996.

Keller, M., and Reiners, W. A.: Soil-atmosphere exchange of nitrous oxide, nitric oxide, and methane under secondary succession of pasture to forest in the Atlantic lowlands of Costa Rica, *Global Biogeochemical Cycles*, *8*(4), 399-409, 1994.

Kim, D.-G., Giltrap, D., and Hernandez-Ramirez, G.: Background nitrous oxide emissions in agricultural and natural lands: a meta-analysis, *Plant Soil*, *373*, 17-30, 2013a.

Kim, D.-G., Hernandez-Ramirez, G., and Giltrap, D.: Linear and nonlinear dependency of direct nitrous oxide emissions on fertilizer nitrogen input: A meta-analysis, *Agriculture, Ecosystems Environment*, *168*, 53-65, 2013b.

Kock, A., and Bange, H. W.: Counting the ocean's greenhouse gas emissions, *Eos: Earth Space Science News*, *96*(3), 10-13, 2015.

Kou Giesbrecht, S., and Arora, V. K.: Representing the dynamic response of vegetation to nitrogen limitation via biological nitrogen fixation in the CLASSIC Land Model, *Global Biogeochemical Cycles*, *36*(6), e2022GB007341, 2022.

Landolfi, A., Somes, C. J., Koeve, W., Zamora, L. M., and Oschlies, A.: Oceanic nitrogen cycling and N2O flux perturbations in the Anthropocene, *Global Biogeochemical Cycles*, *31*(8), 1236-1255, 2017.

Laruelle, G. G., Landschützer, P., Gruber, N., Tison, J.-L., Delille, B., and Regnier, P.: Global high-resolution monthly pCO2 climatology for the coastal ocean derived from neural network interpolation, *Biogeosciences*, *14*(19), 4545-4561, 2017.

Lauerwald, R., Regnier, P., Figueiredo, V., Enrich-Prast, A., Bastviken, D., Lehner, B., Maavara, T., and Raymond, P.: Natural lakes are a minor global source of N2O to the atmosphere, *Global Biogeochemical Cycles*, *33*(12), 1564-1581, 2019.

Le Quéré, C., Buitenhuis, E. T., Moriarty, R., Alvain, S., Aumont, O., Bopp, L., Chollet, S., Enright, C., Franklin, D. J., and Geider, R. J.: Role of zooplankton dynamics for Southern Ocean phytoplankton biomass and global biogeochemical cycles, *Biogeosciences*, *13*(14), 4111-4133, 2016.

Lehner, B., Liermann, C. R., Revenga, C., Vörösmarty, C., Fekete, B., Crouzet, P., Döll, P., Endejan, M., Frenken, K., and Magome, J. : High-resolution mapping of the world's reservoirs and dams for sustainable river-flow management, *Frontiers in Ecology the Environment*, *9*(9), 494-502, 2011.

Lehner, B., Verdin, K., and Jarvis, A.: New global hydrography derived from spaceborne elevation data, *Eos, Transactions American Geophysical Union*, *89*(10), 93-94, 2008.

Lehuger, S., Gabrielle, B., Laville, P., Lamboni, M., Loubet, B., and Cellier, P.: Predicting and mitigating the net greenhouse gas emissions of crop rotations in Western Europe, *Agricultural Forest Meteorology*, *151*(12), 1654-1671, 2011.

Leppelt, T., Dechow, R., Gebbert, S., Freibauer, A., Lohila, A., Augustin, J., Drösler, M., Fiedler, S., Glatzel, S., and Höper, H.: Nitrous oxide emission budgets and land-use-driven hotspots for organic soils in Europe, *Biogeosciences*, *11*(23), 6595-6612, 2014.

Lan, X., E.J. Dlugokencky, J.W. Mund, A.M. Crotwell, M.J. Crotwell, E. Moglia, M. Madronich, D. Neff and K.W. Thoning (2022), Atmospheric Nitrous Oxide Dry Air Mole Fractions from the NOAA GML Carbon Cycle Cooperative Global Air Sampling Network, 1997-2021, Version: 2022-11-21, https://doi.org/10.15138/53g1-x417

Li, C., Aber, J., Stange, F., Butterbach-Bahl, K., and Papen, H.: A process-oriented model of N2O and NO emissions from forest soils: 1. Model development, *Journal of Geophysical Research: Atmospheres*, *105*(D4), 4369-4384, 2000.

Li, C., Frolking, S., and Frolking, T. A.: A model of nitrous oxide evolution from soil driven by rainfall events: 2. Model applications, *Journal of Geophysical Research: Atmospheres*, *97*(D9), 9777-9783, 1992.

Liang, J. H., Deutsch, C., McWilliams, J. C., Baschek, B., Sullivan, P. P., and Chiba, D.: Parameterizing bubble-mediated air-sea gas exchange and its effect on ocean ventilation, *Global Biogeochemical Cycles*, *27*(3), 894-905, 2013.

Lu, C., and Tian, H.: Net greenhouse gas balance in response to nitrogen enrichment: perspectives from a coupled biogeochemical model, *Global Change Biology*, *19*(2), 571-588, 2013.

Maavara, T., Lauerwald, R., Laruelle, G. G., Akbarzadeh, Z., Bouskill, N. J., Van Cappellen, P., and Regnier, P.: Nitrous oxide emissions from inland waters: Are IPCC estimates too high?, *Global Change Biology*, *25*(2), 473-488, 2019.

Madec, G.: NEMO ocean engine: Note du pole de modélisation, Institut Pierre-Simon Laplace (IPSL), France, No 27 ISSN No 1288-1619, *France: IPSL*, 2008.

Madec, G., Bourdallé-Badie, R., Bouttier, P.-A., Bricaud, C., Bruciaferri, D., Calvert, D., Chanut, J., Clementi, E., Coward, A., and Delrosso, D.: NEMO ocean engine, 2017.

Manizza, M., Keeling, R. F., and Nevison, C. D.: On the processes controlling the seasonal cycles of the air–sea fluxes of O2 and N2O: A modelling study, *Tellus B: Chemical Physical Meteorology*, *64*(1), 18429, 2012.

Manizza, M., Menemenlis, D., Zhang, H., and Miller, C. E.: Modeling the recent changes in the Arctic Ocean CO2 sink (2006–2013), *Global Biogeochemical Cycles*, *33*(3), 420-438, 2019.

Martinez-Rey, J., Bopp, L., Gehlen, M., Tagliabue, A., and Gruber, N.: Projections of oceanic N2O emissions in the 21st century using the IPSL Earth system model, *Biogeosciences*, *12*(13), 4133-4148, 2015.

Marzadri, A., Amatulli, G., Tonina, D., Bellin, A., Shen, L. Q., Allen, G. H., and Raymond, P. A.: Global riverine nitrous oxide emissions: The role of small streams and large rivers, *Science of The Total Environment*, *776*, 145148, 2021.

Marzadri, A., Dee, M. M., Tonina, D., Bellin, A., and Tank, J. L.: Role of surface and subsurface processes in scaling N2O emissions along riverine networks, *Proceedings of the National Academy of Sciences*, *114*(17), 4330-4335, 2017.

McCrackin, M. L., Harrison, J. A., and Compton, J. E.: Factors influencing export of dissolved inorganic nitrogen by major rivers: A new, seasonal, spatially explicit, global model, *Global Biogeochemical Cycles*, *28*(3), 269-285, 2014.

Melillo, J. M., Steudler, P. A., Feigl, B. J., Neill, C., Garcia, D., Piccolo, M. C., Cerri, C. C., and Tian, H.: Nitrous oxide emissions from forests and pastures of various ages in the Brazilian Amazon, *Journal of Geophysical Research: Atmospheres*, *106*(D24), 34179-34188, 2001.

Messager, M. L., Lehner, B., Grill, G., Nedeva, I., and Schmitt, O.: Estimating the volume and age of water stored in global lakes using a geo-statistical approach, *Nature Communications*, *7*(1), 13603, 2016.

Nevison, C., Butler, J. H., and Elkins, J. W.: Global distribution of N2O and the ΔN2O-AOU yield in the subsurface ocean, *Global Biogeochemical Cycles*, *17*(4), 2003.

Pan, S., Bian, Z., Tian, H., Yao, Y., Najjar, R. G., Friedrichs, M. A. M., Hofmann, E. E., Xu, R., and Zhang, B.: Impacts of multiple environmental changes on long-term nitrogen loading from the Chesapeake Bay watershed, *Journal of Geophysical Research: Biogeosciences*, *126*(5), e2020JG005826, 2021.

Parekh, P., Joos, F., and Müller, S. A.: A modeling assessment of the interplay between aeolian iron fluxes and iron-binding ligands in controlling carbon dioxide fluctuations during Antarctic warm events, *Paleoceanography*, *23*(4), 2008.

Parton, W. J., Mosier, A. R., Ojima, D. S., Valentine, D. W., Schimel, D. S., Weier, K., and Kulmala, A. E.: Generalized model for N2 and N2O production from nitrification and denitrification, *Global biogeochemical cycles*, *10*(3), 401-412, 1996.

Patra, P. K., Dlugokencky, E. J., Elkins, J. W., Dutton, G. S., Tohjima, Y., Sasakawa, M., Ito, A., Weiss, R. F., Manizza, M., and Krummel, P. B.: Forward and inverse modelling of atmospheric nitrous oxide using MIROC4-atmospheric chemistry-transport model, *Journal of the Meteorological Society of Japan. Ser. II*, *100*(2), 361-386, 2022.

Patra, P. K., Takigawa, M., Watanabe, S., Chandra, N., Ishijima, K., and Yamashita, Y.: Improved chemical tracer simulation by MIROC4. 0-based atmospheric chemistry-transport model (MIROC4-ACTM), *Sola*, *14*, 91-96, 2018.

Paulot, F., Jacob, D. J., Johnson, M. T., Bell, T. G., Baker, A. R., Keene, W. C., Lima, I. D., Doney, S. C., and Stock, C. A.: Global oceanic emission of ammonia: Constraints from seawater and atmospheric observations, *Global Biogeochemical Cycles*, *29*(8), 1165-1178, 2015.

Peltier, W. R.: Global glacial isostasy and the surface of the ice-age Earth: the ICE-5G (VM2) model and GRACE, *Annual Review of Earth and Planetary Sciences*, *32*, 111-149, 2004.

Portmann, F. T., Siebert, S., and Döll, P.: MIRCA2000—Global monthly irrigated and rainfed crop areas around the year 2000: A new high-resolution data set for agricultural and hydrological modeling, *Global Biogeochemical Cycles*, *24*(1), 2010.

Porwollik, V., Rolinski, S., Heinke, J., and Müller, C.: Generating a rule-based global gridded tillage dataset, *Earth System Science Data*, *11*(2), 823-843, 2019.

Prather, M. J., Hsu, J., DeLuca, N. M., Jackman, C. H., Oman, L. D., Douglass, A. R., Fleming, E. L., Strahan, S. E., Steenrod, S. D., and Søvde, O. A.: Measuring and modeling the lifetime of nitrous oxide including its variability, *Journal of Geophysical Research: Atmospheres*, *120*(11), 5693-5705, 2015.

Rochette, P., and Janzen, H. H.: Towards a revised coefficient for estimating N2O emissions from legumes, *Nutrient Cycling in Agroecosystems*, *73*, 171-179, 2005.

Rosentreter, J. A., Laruelle, G. G., Bange, H. W., Bianchi, T. S., Busecke, J. J. M., Cai, W.-J., Eyre, B. D., Forbrich, I., Kwon, E. Y., and Maavara, T.: Coastal vegetation and estuaries are collectively a greenhouse gas sink, *Nature Climate Change*, 1-9, 2023.

Sacks, W. J., Deryng, D., Foley, J. A., and Ramankutty, N.: Crop planting dates: an analysis of global patterns, *Global Ecology Biogeography*, *19*(5), 607-620, 2010.

Salas y Mélia, D.: A global coupled sea ice–ocean model, *Ocean Modelling*, *4*(2), 137-172, 2002.

Séférian, R., Nabat, P., Michou, M., Saint-Martin, D., Voldoire, A., Colin, J., Decharme, B., Delire, C., Berthet, S., and Chevallier, M.: Evaluation of CNRM Earth System Model, CNRM-ESM2-1: role of Earth system processes in present-day and future climate, *Journal of Advances in Modeling Earth Systems*, *11*(12), 4182-4227, 2019.

Shangguan, W., Dai, Y., Duan, Q., Liu, B., and Yuan, H.: A global soil data set for earth system modeling, *Journal of Advances in Modeling Earth Systems*, *6*(1), 249-263, 2014.

Shcherbak, I., Millar, N., and Robertson, G. P.: Global metaanalysis of the nonlinear response of soil nitrous oxide (N2O) emissions to fertilizer nitrogen, *Proceedings of the National Academy of Sciences*, *111*(25), 9199-9204, 2014.

Shu, S., Jain, A. K., Koven, C. D., and Mishra, U.: Estimation of permafrost SOC stock and turnover time using a land surface model with vertical heterogeneity of permafrost soils, *Global Biogeochemical Cycles*, *34*(11), e2020GB006585, 2020.

Solazzo, E., Crippa, M., Guizzardi, D., Muntean, M., Choulga, M., and Janssens-Maenhout, G.: Uncertainties in the Emissions Database for Global Atmospheric Research (EDGAR) emission inventory of greenhouse gases, *Atmospheric Chemistry Physics*, *21*(7), 5655-5683, 2021.

Stehfest, E., and Bouwman, L.: N2O and NO emission from agricultural fields and soils under natural vegetation: summarizing available measurement data and modeling of global annual emissions, *Nutrient cycling in agroecosystems*, *74*, 207-228, 2006.

Sullivan, B. W., Nifong, R. L., Nasto, M. K., Alvarez-Clare, S., Dencker, C. M., Soper, F. M., Shoemaker, K. T., Ishida, F. Y., Zaragoza-Castells, J., and Davidson, E. A.: Biogeochemical recuperation of lowland tropical forest during succession, *Ecology*, *100*(4), e02641, 2019.

Tarantola, A.: *Inverse problem theory and methods for model parameter estimation*, SIAM, 2005.

Thompson, R. L., Chevallier, F., Crotwell, A. M., Dutton, G., Langenfelds, R. L., Prinn, R. G., Weiss, R. F., Tohjima, Y., Nakazawa, T., and Krummel, P. B.: Nitrous oxide emissions 1999 to 2009 from a global atmospheric inversion, *Atmospheric Chemistry Physics*, *14*(4), 1801-1817, 2014.

Thornton, P. E., and Rosenbloom, N. A. : Ecosystem model spin-up: Estimating steady state conditions in a coupled terrestrial carbon and nitrogen cycle model, *Ecological Modelling*, *189*(1-2), 25-48, 2005.

Tian, H., Bian, Z., Shi, H., Qin, X., Pan, N., Lu, C., Pan, S., Tubiello, F. N., Chang, J., and Conchedda, G.: History of anthropogenic Nitrogen inputs (HaNi) to the terrestrial biosphere: a 5 arcmin resolution annual dataset from 1860 to 2019, *Earth System Science Data*, *14*(10), 4551-4568, 2022.

Tian, H., Chen, G., Zhang, C., Liu, M., Sun, G., Chappelka, A., Ren, W., Xu, X., Lu, C., and Pan, S.: Century-scale responses of ecosystem carbon storage and flux to multiple environmental changes in the southern United States, *Ecosystems*, *15*, 674-694, 2012a.

Tian, H., Lu, C., Chen, G., Tao, B., Pan, S., Grosso, S. J. D., Xu, X., Bruhwiler, L., Wofsy, S. C., and Kort, E. A.: Contemporary and projected biogenic fluxes of methane and nitrous oxide in North American terrestrial ecosystems, *Frontiers in Ecology the Environment*, *10*(10), 528-536, 2012b.

Tian, H., Ren, W., Yang, J., Tao, B., Cai, W. J., Lohrenz, S. E., Hopkinson, C. S., Liu, M., Yang, Q., and Lu, C. : Climate extremes dominating seasonal and interannual variations in carbon export from the Mississippi River Basin, *Global Biogeochemical Cycles*, *29*(9), 1333-1347, 2015.

Tian, H., Xu, R., Canadell, J. G., Thompson, R. L., Winiwarter, W., Suntharalingam, P., Davidson, E. A., Ciais, P., Jackson, R. B., Janssens-Maenhout, G., ..., and Yuanzhi, Y.: A comprehensive quantification of global nitrous oxide sources and sinks, *Nature*, *586*(7828), 248-256, 2020a.

Tian, H., Xu, R., Pan, S., Yao, Y., Bian, Z., Cai, W. J., Hopkinson, C. S., Justic, D., Lohrenz, S., and Lu, C.: Long-term trajectory of nitrogen loading and delivery from Mississippi River Basin to the Gulf of Mexico, *Global Biogeochemical Cycles*, *34*(5), e2019GB006475, 2020b.

Tian, H., Xu, X., Liu, M., Ren, W., Zhang, C., Chen, G., and Lu, C.: Spatial and temporal patterns of $CH_4$ and $N_2O$ fluxes in terrestrial ecosystems of North America during 1979–2008: application of a global biogeochemistry model, *Biogeosciences*, *7*(9), 2673-2694, 2010.

Tian, H., Xu, X., Lu, C., Liu, M., Ren, W., Chen, G., Melillo, J., and Liu, J.: Net exchanges of $CO_2$, $CH_4$, and $N_2O$ between China's terrestrial ecosystems and the atmosphere and their contributions to global climate warming, *Journal of Geophysical Research: Biogeosciences*, *116*(G2), 2011.

Tian, H., Yang, J., Lu, C., Xu, R., Canadell, J. G., Jackson, R. B., Arneth, A., Chang, J., Chen, G., and Ciais, P.: The global N2O model intercomparison project, *Bulletin of the American Meteorological Society*, *99*(6), 1231-1251, 2018.

Tschumi, T., Joos, F., Gehlen, M., and Heinze, C.: Deep ocean ventilation, carbon isotopes, marine sedimentation and the deglacial $CO_2$ rise, *Climate of the Past*, *7*(3), 771-800, 2011.

Tsujino, H., Urakawa, L. S., Griffies, S. M., Danabasoglu, G., Adcroft, A. J., Amaral, A. E., Arsouze, T., Bentsen, M., Bernardello, R., and Böning, C. W.: Evaluation of global ocean–sea-ice model simulations based on the experimental protocols of the Ocean Model Intercomparison Project phase 2 (OMIP-2), *Geoscientific Model Development*, *13*(8), 3643-3708, 2020.

Tsujino, H., Urakawa, S., Nakano, H., Small, R. J., Kim, W. M., Yeager, S. G., Danabasoglu, G., Suzuki, T., Bamber, J. L., and Bentsen, M.: JRA-55 based surface dataset for driving ocean–sea-ice models (JRA55-do), *Ocean Modelling*, *130*, 79-139, 2018.

Van Drecht, G., Bouwman, A. F., Harrison, J., and Knoop, J. M.: Global nitrogen and phosphate in urban wastewater for the period 1970 to 2050, *Global Biogeochemical Cycles*, *23*(4), 2009.

Van Drecht, G., Bouwman, A. F., Knoop, J. M., Beusen, A. H. W., and Meinardi, C. R.: Global modeling of the fate of nitrogen from point and nonpoint sources in soils, groundwater, and surface water, *Global Biogeochemical Cycles*, *17*(4), 2003.

Verchot, L. V., Davidson, E. A., Cattânio, H., Ackerman, I. L., Erickson, H. E., and Keller, M.: Land use change and biogeochemical controls of nitrogen oxide emissions from soils in eastern Amazonia, *Global Biogeochemical Cycles*, *13*(1), 31-46, 1999.

Walter, K., Don, A., Fuß, R., Kern, J., Drewer, J., and Flessa, H.: Direct nitrous oxide emissions from oilseed rape cropping–a meta-analysis, *Gcb Bioenergy*, *7*(6), 1260-1271, 2015.

Wang, Q., Zhou, F., Shang, Z., Ciais, P., Winiwarter, W., Jackson, R. B., Tubiello, F. N., Janssens-Maenhout, G., Tian, H., and Cui, X.: Data-driven estimates of global nitrous oxide emissions from croplands, *National Science Review*, *7*(2), 441–452, 2020.

Wanninkhof, R.: Relationship between wind speed and gas exchange over the ocean, *Journal of Geophysical Research: Oceans*, *97*(C5), 7373-7382, 1992.

Wanninkhof, R.: Relationship between wind speed and gas exchange over the ocean revisited, *Limnology Oceanography: Methods*, *12*(6), 351-362, 2014.

Weiss, R. F., and Price, B. A.: Nitrous oxide solubility in water and seawater, *Marine Chemistry*, *8*(4), 347-359, 1980.

Wells, K. C., Millet, D. B., Bousserez, N., Henze, D. K., Chaliyakunnel, S., Griffis, T. J., Luan, Y., Dlugokencky, E. J., Prinn, R. G., and O'Doherty, S.: Simulation of atmospheric N 2 O with GEOS-Chem and its adjoint: evaluation of observational constraints, *Geoscientific Model Development*, *8*(10), 3179-3198, 2015.

Wilson, C., Chipperfield, M. P., Gloor, M., and Chevallier, F.: Development of a variational flux inversion system (INVICAT v1. 0) using the TOMCAT chemical transport model, *Geoscientific Model Development*, *7*(5), 2485-2500, 2014.

Wollheim, W. M., Vörösmarty, C. J., Bouwman, A. F., Green, P., Harrison, J., Linder, E., Peterson, B. J., Seitzinger, S. P., and Syvitski, J. P. M.: Global N removal by freshwater aquatic systems using a spatially distributed, within-basin approach, *Global Biogeochemical Cycles*, *22*(2), 2008.

Xu-Ri, and Prentice, I. C.: Terrestrial nitrogen cycle simulation with a dynamic global vegetation model, *Global Change Biology*, *14*(8), 1745-1764, 2008.

Xu, R., Tian, H., Lu, C., Pan, S., Chen, J., Yang, J., and Zhang, B.: Preindustrial nitrous oxide emissions from the land biosphere estimated by using a global biogeochemistry model, *Climate of the Past*, *13*(7), 977-990, 2017.

Xu, X., Sharma, P., Shu, S., Lin, T.-S., Ciais, P., Tubiello, F. N., Smith, P., Campbell, N., and Jain, A. K.: Global greenhouse gas emissions from animal-based foods are twice those of plant-based foods, *Nature Food*, *2*(9), 724-732, 2021.

Xu, X., Tian, H., Liu, M., Ren, W., Chen, G., Lu, C., and Zhang, C.: Multiple-factor controls on terrestrial N2O flux over North America from 1979 through 2010, *Biogeosciences Discussions*, *8*(6), 2011.

Yang, H., Zhou, F., Piao, S., Huang, M., Chen, A., Ciais, P., Li, Y., Lian, X., Peng, S., and Zeng, Z.: Regional patterns of future runoff changes from Earth system models constrained by observation, *Geophysical Research Letters*, *44*(11), 5540-5549, 2017.

Yang, Q., Tian, H., Friedrichs, M. A. M., Hopkinson, C. S., Lu, C., and Najjar, R. G.: Increased nitrogen export from eastern North America to the Atlantic Ocean due to climatic and anthropogenic changes during 1901–2008, *Journal of Geophysical Research: Biogeosciences*, *120*(6), 1046-1068, 2015.

Yang, S., Chang, B. X., Warner, M. J., Weber, T. S., Bourbonnais, A. M., Santoro, A. E., Kock, A., Sonnerup, R. E., Bullister, J. L., and Wilson, S. T.: Global reconstruction reduces the uncertainty of oceanic nitrous oxide emissions and reveals a vigorous seasonal cycle, *Proceedings of the National Academy of Sciences*, *117*(22), 11954-11960, 2020.

Yang, X., Wittig, V., Jain, A. K., and Post, W.: Integration of nitrogen cycle dynamics into the Integrated Science Assessment Model for the study of terrestrial ecosystem responses to global change, *Global Biogeochemical Cycles*, *23*(4), 2009.

Yao, Y., Tian, H., Shi, H., Pan, S., Xu, R., Pan, N., and Canadell, J. G.: Increased global nitrous oxide emissions from streams and rivers in the Anthropocene, *Nature Climate Change*, *10*(2), 138-142, 2020.

Yao, Y., Tian, H., Xu, X., Li, Y., and Pan, S.: Dynamics and controls of inland water $CH_4$ emissions across the Conterminous United States: 1860-2019, *Water Research*, *224*, 119043, 2022.

Yool, A., Martin, A. P., Fernández, C., and Clark, D. R.: The significance of nitrification for oceanic new production, *Nature*, *447*(7147), 999-1002, 2007.

Zaehle, S., Ciais, P., Friend, A. D., and Prieur, V.: Carbon benefits of anthropogenic reactive nitrogen offset by nitrous oxide emissions, *Nature Geoscience*, *4*(9), 601-605, 2011.

Zaehle, S., and Friend, A. D.: Carbon and nitrogen cycle dynamics in the O-CN land surface model: 1. Model description, site-scale evaluation, and sensitivity to parameter estimates, *Global Biogeochemical Cycles*, *24*(1), 2010.

Zamora, L. M., and Oschlies, A.: Surface nitrification: A major uncertainty in marine $N_2O$ emissions, *Geophysical Research Letters*, *41*(12), 4247-4253, 2014.

Zhang, Y., Li, C., Zhou, X., and Moore III, B.: A simulation model linking crop growth and soil biogeochemistry for sustainable agriculture, *Ecological Modelling*, *151*(1), 75-108, 2002.

Zhou, F., Shang, Z., Zeng, Z., Piao, S., Ciais, P., Raymond, P. A., Wang, X., Wang, R., Chen, M., and Yang, C.: New model for capturing the variations of fertilizer-induced emission factors of $N_2O$, *Global Biogeochemical Cycles*, *29*(6), 885-897, 2015.

Zhou, J. B., Jiang, M. M., and Chen, G. Q.: Estimation of methane and nitrous oxide emission from livestock and poultry in China during 1949–2003, *Energy Policy*, *35*(7), 3759-3767, 2007.

Zhu, Q., Riley, W. J., Tang, J., and Koven, C. D. : Multiple soil nutrient competition between plants, microbes, and mineral surfaces: model development, parameterization, and example applications in several tropical forests, *Biogeosciences*, *13*(1), 341-363, 2016.